Astronomy & Astrophysics manuscript no. output
February 19, 2026

Multi-epoch afterglow re-brightenings in GRB 250129A: evidence for successive shock interactions

D. Akl [1,2,64], S. Antier [1,3], H. Koehn [47], P. T. H. Pang [48,49],⋆ J.J. Geng [23],⋆⋆ R. Gill [46],⋆⋆⋆ N. Globus [32], E. Abdikamalov [69,70], C. Adami [14], V. Aivazyan [4], L. Almeida [27,28], S. Alshamsi [60], F. Alvarez [18], C. Andrade [9], Q. André,[1], C. Angulo [18], J.-L. Atteia [36], K. Barkaoui [42,41,40], S. Basa [15], R.L. Becerra [21], P. Bendjoya [43], D. Berdikhan [70], E. Bernaud [15], D. Bieerdehan [69,70], S. Boissier [15], S. Brunier [43], A.Y. Burdanov [40], N.R. Butler [19], J. Chen [23,24], F. Colas [44], M.W. Coughlin [9], D. Darson [57], T. Dietrich [47,50], D. Dornic [20], C. Douzet [3], C. Dubois [15], J.-G. Ducoin [20], T. du Laz [53], A. Durroux,[1], D. Dutton [6], P.-A. Duverne [10], F. Du[illegible] [35], A. Esamdin [54,55], A.V. Filippenko [26], F. Fortin [36], M. Freeberg,[37], L. García-García [18], [illegible]Gillon [41], P. Gokuldass [58], N. Guessoum [60], P. Hello [3], R. Hellot [33], Y. Hendy [12], Y.L. Hua [23,24], T. Hussenot-Desenonges [3], R. Inasaridze [4], A. Iskandar [54,55], M. Jelínek [30], S. Karpov [11], A. Klotz [36], N. Kochiashvili [4], T. Laskar [51,52], A. Le Calloch [9], W.H. Lee [18], S. Leonini [31], X.Y. Li [25], A. Lien [67,68], C. Limonta [1], J. Liu [56], D. López-Cámara [45], F. Magnani [20], J. Mao [65] M. Mašek [11], E. Moreno Méndez [22], L.C. Menegazzi [50], W. Mercier [15], B.M. Mihov [7], M. Molham [12], S. Oates [38], M. Odeh,[38], H. Peng,[56], M. Pereyra [18], M. Pillas [5], T. Pradier [13], N.A. Rakotondrainibe [15], D. Reichart [6], J.-P. Rivet [43], F. Romanov, A. Saccardi [16], N. Sasaki [59], D. Schlekat [6], B. Schneider [15], A. Simon [61], L. Slavcheva-Mihova [7], R. Strausbaugh [17], T.R. Sun [23], A. Takey,[12], M. Tanasan,[62], D. Turpin [14], A. de Ugarte Postigo [15], L.T. Wang,[56], X.F. Wang [56], Z.M. Wang [66], A.M. Watson [18], J. de Wit [40], Y.S. Yan [56], W. Zheng [26], S. Zúñiga-Fernández [41]

(Affiliations can be found after the references)

Received ...; accepted ...

ABSTRACT

Context. Most long gamma-ray bursts (GRBs) exhibit afterglows broadly consistent with external forward-shock emission, typically described by smooth broken power-law decays in the multi-band light curve. However, a minority of well-sampled GRBs deviate from this behavior, as the GRB we are investigating in this article, GRB 250129A. The latter shows multiple late-time rebrightenings in the X-ray and optical wavelengths. Rebrightenings are often attributed to energy injection from prolonged central engine activity, refreshed shocks from delayed shell collisions, density jumps in the ambient medium, or angular jet structure and viewing-angle effects.
Aims. After a comprehensive analysis of the prompt emission of the GRB observed in gamma-rays and near-infrared, we aim to investigate the physical origin of the multiple X-ray and optical flaring episodes observed in GRB 250129A.
Methods. We conduct comprehensive temporal and spectral multi-band analyses of GRB 250129A. The physical processes at play in the afterglow light curves was investigated using several methods, ranging from empirical fitting to Bayesian inference. The high-quality monitoring of the flare episodes, together with the connection between the prompt emission and the afterglow, enables us to test the consistency of the fireball model and to constrain, reject, or confirm alternative scenarios.
Results. GRB 250129A is an interesting GRB with multi-wavelength prompt and afterglow emissions. C[illegible]ting the prompt and time-resolved analyses, we obtained an isotropic-equivalent energy of $E_{\rm iso,\gamma} = (1.35 \pm 0.12) \times 10^{53}$ erg. By modeling t[illegible]rglow using an agnostic Bayesian framework (NMMA), we rule out both a single external-shock evolution and a one-time energy injection scenario. By further performing numerical calculations, we demonstrate that the rebrightening episodes are consistent with refreshed shocks arising from delayed collisions between relativistic shells, in agreement with evolving outflow dynamics.
Conclusions. Thanks to the consistency between our prompt and afterglow analyses of GRB 250129A, together with prior literature on micro-physical properties, we conclude that at least two statistically significant rebrightening episodes can be explained by a sequence of refreshed-shock scenarios. We emphasize that the availability of timely and spectrally rich GRB datasets, as presented in this work, provides a valuable means to challenge current modeling frameworks.

Key words. gamma-ray burst: individual: GRB 250129A – transients: gamma-ray bursts

1. Introduction

Gamma-ray bursts (GRBs) are among the most luminous and violent electromagnetic phenomena observed in the universe (Piran 2004; Kumar & Zhang 2015). Based on their T_{90} duration, defined as the time interval over which the central 90% of the gamma-ray fluence is accumulated, they are classified into two categories, short ($T_{90} < 2$ s) or long ($T_{90} > 2$ s) GRBs (Kouveliotou et al. 1993; Steinhardt et al. 2023) as exemple. A large fraction of long GRBs is suggested to originate from the collapse of massive stars, as confirmed through associations with broad-line Type Ic super-

⋆ Corresponding author: e-mail: thopang@nikhef.nl
⋆⋆ Corresponding author: e-mail: jjgeng@pmo.ac.cn
⋆⋆⋆ Corresponding author: e-mail: r.gill@irya.unam.mx

novae (Woosley 1993; MacFadyen & Woosley 1999; Woosley & Heger 2012; Hussenot-Desenonges et al. 2024; Srinivasaragavan et al. 2024), although a subset may originate from alternative progenitors (Rastinejad et al. 2022; Luo et al. 2023; Neights et al. 2025). In contrast, short gamma-ray bursts are mostly caused by the merging of compact objects (Paczynski 1986; Eichler et al. 1989; Paczyński 1991; Narayan et al. 1992), as evidenced by their joint detections of associated kilonovae and gravitational waves (Abbott et al. 2017; Cano et al. 2017).

One of the most favored explanations for GRBs is the *fireball* scenario (Meszaros & Rees 1993; Waxman & Piran 1994; Piran 1999a; Kumar & Zhang 2015), in which the prompt gamma-ray emission arises from energy dissipation within a narrow relativistic jet due to internal shocks produced by collisions between discrete shells with different velocities. The jet is decelerated through its interaction with the external medium, driving an external forward shock that produces the long-lasting and broadband (radio to X-rays) synchrotron afterglow emission. Following deceleration, the afterglow emission typically declines over time as a power law in the X-ray and optical bands when they originate from the same power-law segment of the synchrotron spectrum. Although fireball dynamics are often approximated as spherical at early times, the outflow is in fact collimated into a jet of half-opening angle θ_j. As the blast wave decelerates, the relativistic beaming angle (with size $1/\Gamma$) increases and eventually exceeds θ_j, causing the jet edge to become visible and allowing lateral expansion to set in. This leads to the characteristic steepening of the afterglow light curve known as the jet break (Rhoads 1999; Sari et al. 1999).

The light curve of GRB afterglows is expected to follow a smooth temporal evolution; however, intense, rapid rebrightenings (or flares), gradual ones lasting over minutes to days, and other irregularities in the multi-band afterglow light curve are often revealed in a fraction of high-cadence GRBs with well-sampled multi-band observations (Nousek et al. 2006a; Evans et al. 2009; Liang et al. 2013; Kumar & Zhang 2015; de Ugarte Postigo, A. et al. 2018; Busmann et al. 2025). Between 20 and 30% of long GRBs exhibit optical rebrightenings in their afterglow (e.g., Li et al. 2012; Becerra et al. 2023).

One possible explanation includes energy injection into the blast wave due to the expulsion of multiple shells by the central engine that later collide and produce a rapid brightening of the afterglow (Panaitescu et al. 1998; Rees & Meszaros 1998; Kumar & Piran 2000; Sari & Mészáros 2000; Zhang & Mészáros 2002; Uhm et al. 2012; Laskar et al. 2015a; Fraija et al. 2022; Moss et al. 2023). The GRB central engine is expected to be highly variable, and the expulsion of late shells may be associated with fall-back of material onto the central engine (MacFadyen et al. 2001). Late-time energy injection has been used to explain observed plateaus and rebrightenings in a substantial number of GRBs (Nousek et al. 2006b; Yu et al. 2007; Margutti et al. 2010; Laskar et al. 2015a).

Alternatively, energy can be added to the blast wave gradually and continuously. This can occur when the ejecta has a radial velocity gradient (Granot & Kumar 2006; Zhang et al. 2006; van Eerten 2018; Ryan et al. 2020), with progressively slower-moving inner shells trailing behind the faster moving outer shell, or if the central engine is a magnetar that injects energy continuously into the blast wave via a magnetohydrodynamic (MHD) pulsar-type wind (Dai & Lu 1998; Zhang & Mészáros 2001, 2002; Geng et al. 2016). In both scenarios, the afterglow light curve shows an achromatic bump or rebrightening as the energy is injected, with the post-injection light curve following the same temporal decay as that of the pre-injection one in the absence of spectral break passage. Multiple rebrightening episodes are are generally not expected in this scenario.

Such multiple episodes can instead been explained by having an asymmetric structured jet, where different azimuthal jet components, with distinct energies and Lorentz factors, sequentially dominate the afterglow emission, producing multiple peaks (Li et al. 2024).

Another possible explanation is a non-uniform circumburst environment in which the blast wave encounters density enhancements that could lead to rebrightenings (Wang & Loeb 2000; Dai & Lu 2002; Uhm & Zhang 2014). These density structures may be organized as spherical shells formed by unstable wind episodes of the progenitor or clumpy remnant of a previous supernova explosion, a scenario consistent with constraints from multiwavelength imaging and spectroscopy (Wang & Loeb 2000; Lazzati et al. 2002; Huang et al. 2006). However, analytic calculations (Nakar & Granot 2007) and numerical simulations (van Eerten et al. 2009) show that even large density enhancements will only produce a mild rebrightening in the light curve.

In this paper, we present multi-waveband observations of GRB 250129A that was detected by the Burst Alert Telescope *Swift*/BAT instrument on the *Neil Gehrels Swift Observatory* at T_0 = 2025 January 29 04:45:09 UTC (Beardmore et al. 2025) (trigger num: 1285812, SNR in the image trigger of 10.13, duration of the trigger: 64s in the 15 - 50 KeV energy band). It was simultaneously detected by *Konus-Wind* from T_0-66 s to T_0+208s in the [20 - 400] keV with detection significance above 6σ (Frederiks et al. 2025). The GRB was classified as a long burst with a duration of T_{90} = 262.25 ± 23.71 seconds as determined by the online analysis in the 15-350 keV band. *Swift* initiated an automatic slew and performed follow-up observations with the X-Ray Telescope *Swift*/XRT and the Ultra-Violet and Optical Telescope *Swift*/UVOT (see Roming et al. 2005) (Siegel et al. 2025) mencing at T_0 + 158.6 s. Both X-ray and optical counter were found: the first follow-up revealed an uncatalogued X-ray source located 54 arcseconds from the BAT position (Beardmore et al. 2025) and a candidate optical afterglow with a magnitude of 17.88, positioned within 2.7 arcseconds of the XRT localization, in the white filter (Beardmore et al. 2025).

Various follow-up observations were initiated rapidly, beginning as early as 1.9 minutes after T_0, while the prompt emission was ongoing, and observations continued over several weeks. These efforts involved about 30 ground-based telescopes and instruments. For instance, early optical imaging was conducted by the OHP-T193 cm telescope, 30 minutes after the *Swift*/BAT trigger (Schneider et al. 2025b) and the Las Cumbres Observatory Global Telescope (Ghosh et al. 2025) 1.17 hr post-trigger; while extended monitoring was carried out by the 2m robotic Liverpool Telescope and the SAO RAS 1-m telescope, ∼ 24.1 hr and ∼ 43.298 hr after the trigger, respectively (Bochenek & Perley 2025; Moskvitin et al. 2025) (see all GCN reports). Observations were also conducted by the COLIBRI telescope (Watson et al. 2025a; Akl et al. 2025a; Watson et al. 2025b), as well as the Global Rapid Advanced Network Devoted to Multi-messenger Addicts (GRANDMA) (Antier et al. 2020) and its citizen science program, Kilonova-Catcher (KNC) (Antier et al. 2025; Akl et al. 2025b) (see the GRB 250129A SkyPortal Public Page to retrieve results submitted by various teams. Note that these are uncorrected for the extinctions.

The first observations showed a steep optical and X-ray rebrightening within the first day, a feature that cannot be accounted for by a standard fireball afterglow model (**?**Zhang et al. 2006), and thus motivated long-term follow-up that revealed additional rebrightening episodes. GRB250129A redshift was also mea-

sured at $z = 2.151$ from VLT/X-shooter at $T - T_0 = 1.315$ hours (Schneider et al. 2025a): the observations revealed Lyα absorption at ~3830Å, along with absorption lines from ions such as SiII, CIV, and FeII. This redshift was later confirmed by the Nordic Optical Telescope (NOT)'s (Izzo et al. 2025), and the MISTRAL spectro-imager at Observatoire de Haute-Provence (Schneider et al. 2025c).

We performed a multi-stage modeling analysis of the GRB 250129A afterglow to probe the physical origin of its rebrightening episodes, investigating mechanisms linked to central energy reactivation. We focus on scenarios involving energy injection into the forward shock and a series of refreshed shocks produced by collisions between shells with different bulk Lorentz factors launched during the prompt phase.

The paper is structured as follows. In §2, we present the observational data set, including the prompt emission and multi-wavelength afterglow data from gamma-ray, X-ray, optical, and UV observations. In §3, we perform an analysis of the dust environment and the possible host galaxy. In §4, we present the theoretical modeling and physical interpretation of the event based on various jet structure scenarios. Finally, we summarize our conclusions in §5.

2. Observational dataset

2.1. Prompt Observations

Gamma-Ray – We analyzed the temporal and spectral characteristics of the GRB prompt emission observed by *Swift*/BAT. Mask-weighted light curves (binned to a signal-to-noise ratio of 5) and spectra were constructed using `batbinevt`. We defined four burst intervals based on the edges obtained from the Bayesian block algorithm (Scargle et al. 2013) and the rise and decay slopes of the pulses, as shown in the top panel of Figure 1.

Time-resolved spectra were extracted for the four intervals, and the spectral models were selected between a single power-law (SPL) and a cutoff power-law (CPL) using Bayesian Information Criterion (BIC) tests, requiring an improvement of ΔBIC = 4. Intervals 1, 2, and 4 are best fitted by SPL models, while Interval 3 is best fitted by a CPL model with $\alpha = -1.20^{+0.25}_{-0.24}$ and $E_0 = 42^{+17}_{-10}$ keV, which is consistent to the result reported by *Konus–Wind* (Frederiks et al. 2025). The time-resolved spectra as well as corresponding intervals are shown in Figure 2. Based on the best-fit spectral models, the photon counts were subsequently converted to the flux density at 10 keV, as shown in Figure 1.

Accounting for the cosmological k-correction (Bloom et al. 2001), we calculate an isotropic-equivalent energy of $E_{\mathrm{iso},\gamma} = (1.35 \pm 0.12) \times 10^{53}$ erg by summing the fluence over the four intervals.

Optical Observations During the Prompt Emission – The Télescopes à Action Rapide pour les Objets Transitoires (TAROT)[1] associated with the GRANDMA collaboration started observing the GRB about 106 seconds after T_0 in drift mode and without filter (e.g, the tracking of the hour-angle motor was adapted to a drift of 0.30 pixel/s), enabling a record of the flux during 60 s without dead time (Klotz et al. 2006). This sequ covering the prompt emission during about 70 s, is show Figure 1.

[1] `http://tarot.obs-hp.fr/`

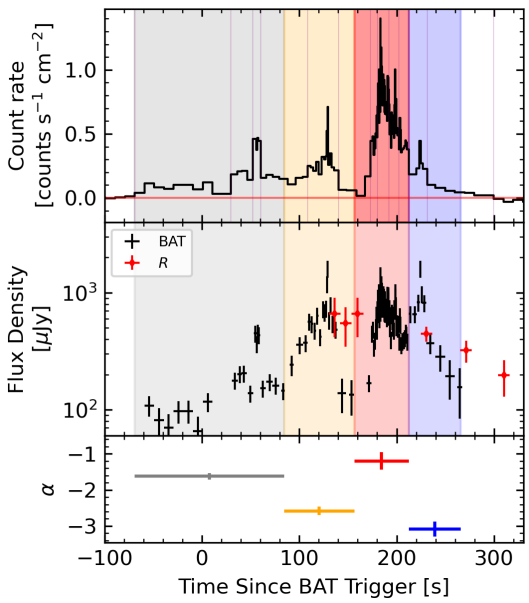

Fig. 1. Top: *Swift*/BAT mask-weighted count-rate light curve with Bayesian block edges. Middle: *Swift*/BAT (10 keV) and TAROT R-band flux density light curves. Bottom: Best-fit spectral indices.

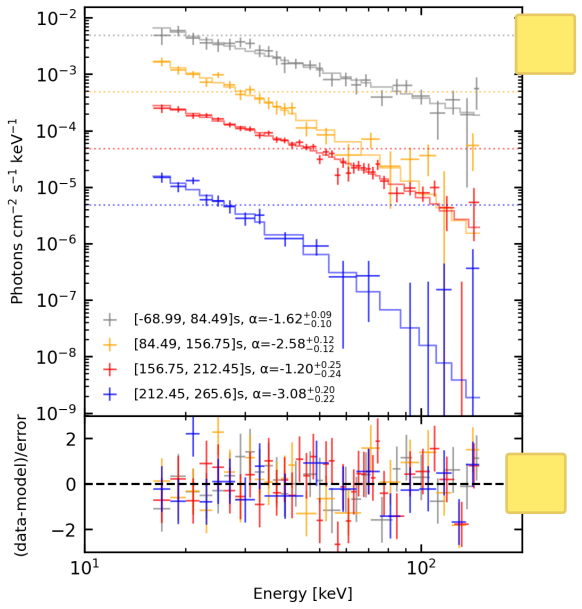

Fig. 2. BAT 15–150 keV time-resolved spectra and best-fit models for GRB 250129A. For clarity, the fluxes of successive intervals are scaled by a constant factor of 0.1 relative to the previous interval; the horizontal dashed lines indicate the reference flux levels of the first interval. The fit results are reported with 90% confidence intervals. "0" corresponds to the time of the trigger T_0.

2.2. X-ray Afterglow

Light curve – We retrieved the XRT unabsorbed flux density light curves resampled for the 10 keV band from the `Burst Analyser`[2]. We rebinned the light curve by grouping data points into 16 manually defined, non-contiguous clusters based on temporal proximity to improve the signal-to-noise ratio while pre-

[2] `https://www.swift.ac.uk/burst_analyser/01285812/`

serving the time evolution. Among these, 4 bins contained clusters of 2–5 closely spaced observations, while the remaining bins contained a single point each. For each bin, we computed the mean magnitude and standard deviation. We then converted the flux density from 10 keV to 2 keV (see Appendix C), to ensure our analysis is grounded in the energy range where *Swift*-XRT is most sensitive. The light curve can be seen in Figure 5, and all the data are available in SkyPortal and in Table D.2 of the Appendix.

Time resolved spectra – We extracted the spectral characteristics in the [0.3-10 keV] range of *Swift*-XRT data in various epochs (see Figure 3). The data reduction and spectral analysis were conducted in the same approach for all the epochs using `HEASoft v6.34`, and processed using the `XRT tool xrtpipeline (v0.13.7)`. The spectra were fitted with an absorbed power-law model, leaving only the photon index (Γ) and the normalization as free parameters, with the galactic column density ($N_H = 2.4 \times 10^{20}$ cm^{-2}) fixed[3]. Spectral modeling and parameter estimation were performed using standard processing (See Appendix C).

We first investigated potential spectral evolution within the first day following the discovery from 2025-01-29T05:04:40 to 2025-01-29T18:49:13, as the low count rate after the first day prevented the fitting for properties such as the photon index. The best-fit photon indices for the three source spectra within the first day shared the same characteristics with the photon index $\Gamma = 1.99 \pm 0.23$, $\Gamma = 2.15 \pm 0.15$, and $\Gamma = 1.87 \pm 0.18$, respectively. We then analyzed one epoch more carefully, which corresponds to high variation in optical. We split the period [0.061–0.197] post T_0 at $T = 0.061$, which coincides with a transition in the optical light curve from a rising to a decaying phase. Separate spectral fits were performed for each using the same method outlined in Appendix C. The resulting photon indices were $\Gamma = 2.22 \pm 0.18$ for the rising phase and $\Gamma = 2.11 \pm 0.34$ for the decaying phase. While the values differ slightly, the uncertainties overlap significantly, indicating no statistically significant spectral evolution during this period. This is further discussed by fitting the spectral energy distribution (SED), as detailed in Sec 3.1.

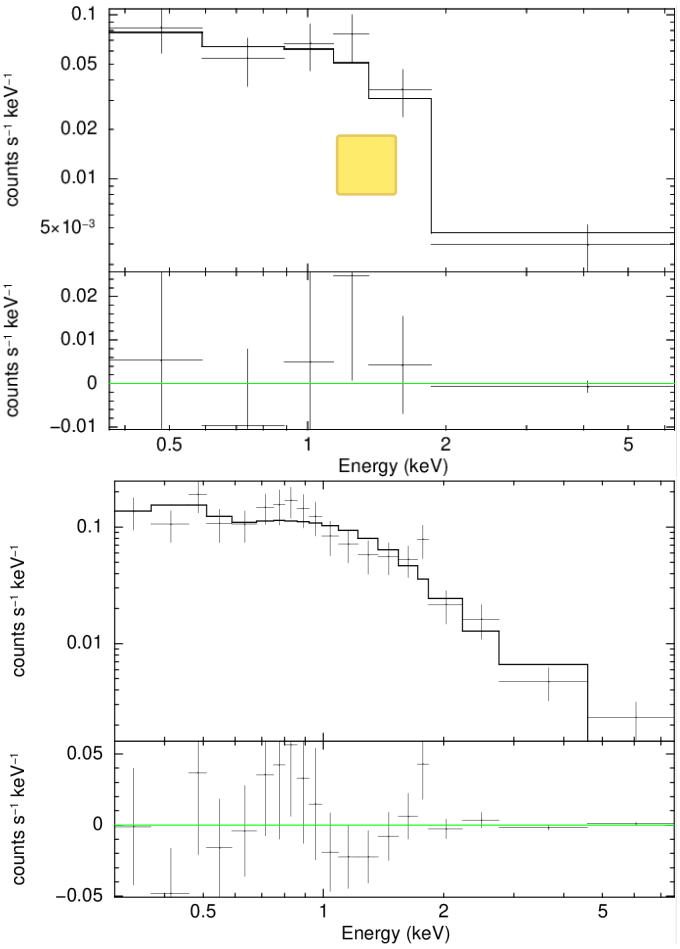

Fig. 3. X-ray spectra fitted with a power-law (PL) model. **Top panel:** Spectrum from the decay interval of observation ID `01285812001`, corresponding to $T - T_0 = 0.1355$ to 0.1969 days. **Bottom panel:** Spectrum from the rise interval of the same observation, spanning $T - T_0 = 0.061$ to 0.1355 days.

2.3. UVOIR Afterglow

Space – We performed aperture photometry in $UVW1$, $UVW2$, $UVM2$ (ultraviolet), and U, B, V (optical) to extract the *Swift*/UVOT light curve using a 5″-radius circular source region and a 15″-radius background region away from the source. For individual exposures, we employed the `uvotmaghist` task. In addition, we selectively co-added exposures that were close in time within a range of a couple of minutes in the same band, identified based on their temporal distribution on a log-time scale plot. These subsets were summed using `uvotimsum`, and photometry was then performed using `uvotsource`. This approach allowed us to preserve time resolution where needed and improve signal-to-noise ratio, as well as decrease uncertainty and error, particularly with the exposures that were clustered closely in time.

Very early-time exposures initially excluded by `uvotmaghist` due to failed aspect correction (i.e., `ASPCORR` keyword set to `NONE`) were manually corrected using `uvotaspcorr` to allow for their inclusion. The initial V-band settling image was also examined for detector ramp-up effects. To assess its reliability, we compared the photometry of field stars in the settling image with that from later stacked V-band exposures. Additionally, we considered non-detection when the signal-to-noise is under 2, which is typically associated with contamination from known internal dust regions within the telescope. All the UVOT data are available in Table D.3 and shown in Figure 5.

Ground – The processing of all optical observations of the 30 different instruments at play followed the same methodologies to maintain consistency and data quality. The pre-processing after data acquisition started with bias and dark subtraction, as well as flat-field correction according to each telescope's specifics. We then manually masked areas within each image with visible imaging artifacts or areas that were not entirely corrected during pre-processing (especially at the edges). We verified or derived astrometric solutions using the `astrometry.net` service (Lang et al. 2010), on either individual images or stacked images. We performed dynamical image stacking using the SWarp software (Bertin 2010) to retain high temporal resolution and a signal-to-noise ratio above 3 at the location of the transient.

Forced photometry of all the stacked images (e.g, ~ 290 images) was performed at the transient position (e.g, RA, Dec: 198.676728, 5.030631) using `STDPipe` (Karpov 2021; Karpov 2025), a home-made Python-based set of codes for performing

[3] `https://www.swift.ac.uk/xrt_spectra/01285812/`

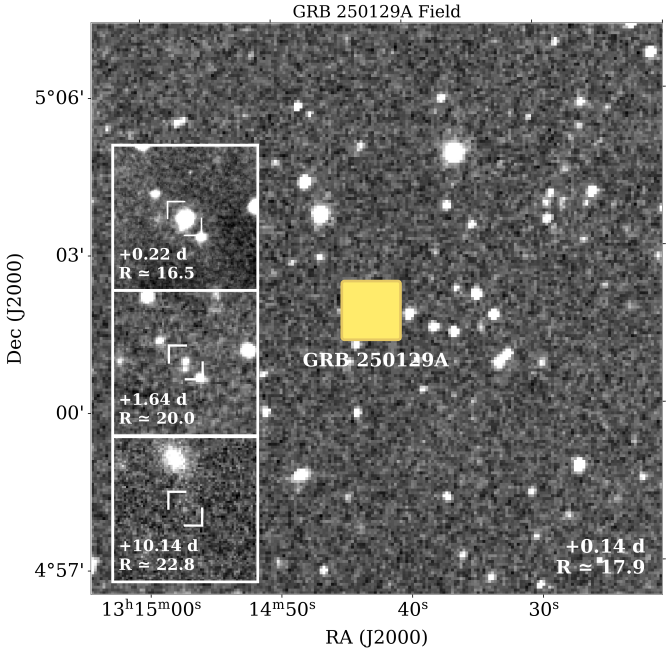

Fig. 4. TAROT-TCH telescope image of GRB 250129A taken at $T - T_0 = 0.14$ d. The insets show the zoomed-in region of three images from the KAIT, Abastumani-T70, and Euler telescopes centered on the GRB location, taken at phases of $T - T_0 = 0.22$, $T - T_0 = 1.64$, and $T - T_0 = 10.14$ d, respectively, relative to the *Swift* GRB trigger (MJD 60704.198).

astrometry, photometry, and transient detection tasks on optical images, originally created as part of the GRANDMA Collaboration. We utilized the associated web interface `STDWeb`[4] to conduct our photometry and seek for anomalies that need further adjustments (e.g., high background noise, calibration issues, etc). Catalogs for the photometric calibration were chosen based on the filters used to acquire the images. Instrumental magnitudes were calibrated using the Gaia DR3 Synthetic Photometry Catalog (Gaia Collaboration et al. 2023) and Pan-STARRS Data Release 1 catalog (Chambers et al. 2016) for images obtained in filters close to the Johnson-Cousins filter system (U, B, V, Rc, Ic) and Sloan filters (g, r, i, z), respectively. Images obtained using non-standard filters (not part of the Johnson-Cousins or Sloan systems) were calibrated using the filter and catalogue, which minimized the color term [5] to below 0.1. Particularly, unfiltered images are challenging since they cover the full wavelength range.

Specific treatment of several images was required to correctly calibrate them using standard catalogs. For example, a first non-linear color term was needed to adjust the data of the early afterglow ($T - T_0 < 0.2$ day): the color term estimation had to be modified into a parabolic color term, which was then used to fit both datasets from the TAROT/TCH and FRAM-Auger telescopes. Specifically, the correction for the color we obtained is $B - V = 1.46$ ($\sim g - r = 1.27$). Hence, the color term was applied to TAROT/TCH as $[R + 0.44(B - V) - 0.29(B - V)^2]$ and to FRAM-Auger data as $[R + 0.06(B - V)]$. As shown in Figure 5, the results are compatible in the R-band. We additionally added data from Skynet telescopes in the B-, V-, R-, and I-bands, and we applied a joint color correction of $(B - V) = 0.4$ to Skynet, TAROT/TCH, and FRAM-Auger to minimize the offsets introduced by the distinct filter responses of the telescopes. This correction indicated that the transient exhibited a relatively blue color of $(B - V) = 0.4$ during the early-time window, thereby superseding our earlier interpretation that the transient was red at early times.

At later times, from $0.2 < T - T_0 < 1$ days, the analysis of KAIT data taken without a filter was challenging due to poor background quality and high noise levels in certain images; no color term corrections were applied as their inclusion led to further instability in the fit. To mitigate these issues, the number of free parameters was minimized: the background mesh size, or the size of the grid cells used for global background estimation, was reduced to 32 pixels, with a constant zero-point, and a reduced annulus size was constrained to apertures of 2 and 4 FWHM for the sky inner and outer annuli, respectively.

Finally, when the afterglow reached a magnitude above 21.5 magnitude, we subtracted a template image from the Legacy DESI Survey Data Release 10[6] to isolate the flux contribution using High Order Transform of Psf and a template subtraction code `HOTPANTS` (Becker 2015) algorithm for image subtraction.

Besides, observations included one infrared J-band image obtained by the Pic Du Midi telescope; however, this data point was not used in the offline analysis as it only included one upper limit.

3. Environment

3.1. Host galaxy line-of-sight extinction

The line-of-sight host galaxy dust extinction has been estimated by creating an X-ray-to-optical spectral energy distribution (SED) using *Swift*/XRT and optical data ($g'r'i'z'$), corrected from the Galactic reddening of $E(B - V) = 0.03$ mag (Schlafly & Finkbeiner 2011b), at a mid-time of $T - T_0 \sim 7.04$ days after the *Swift* trigger, where no further spectral evolution is observed. We note that due to the absence of NIR data to construct the SED, the estimated extinction might be underestimated. Indeed, determining optical extinction becomes more complex without NIR observations, as they are less affected by dust than bluer wavelengths. Moreover, they can also serve as crucial anchors in constraining the intrinsic spectral shape of the afterglow.

Compared to section 2.2, we retrieved the time-sliced X-ray spectrum, covering the 2.22-12.74 days interval, keeping high timing resolution and directly from the automated data products provided by the public *Swift*/XRT archive (Evans et al. 2007). Photometric data in the $g'r'i'z'$ bands from section 2.3 were interpolated to the common reference time of the z'−band (e.g MJD 60711.237) at ∼7.04 days after the trigger. The SED fit was performed by following a standard routine using the average extinction curves of the Milky Way (MW), Large (LMC), and Small Magellanic (SMC) Clouds (Pei 1992), and the intrinsic X-ray-to-optical spectrum was modeled with a single or broken power-law according to the shape of the afterglow theory (Sari et al. 1998). The slope of the X-ray wavelengths was assumed to be 0.5 steeper than the spectral slope below the cooling break of the intrinsic spectra, i.e., $\Delta\beta = \beta_X - \beta_o = 0.5$. We fixed the redshift and the Galactic foreground absorption of $N_H^{Gal} = 2.43 \times 10^{+20}$ cm^{-2} (Willingale et al. 2013; HI4PI Collaboration et al. 2016).

A simple power law model with the MW extinction curve gives a fit with the parameters $\beta = 1.15^{+0.13}_{-0.04}$, $E(B - V) =$

[4] Accessible at `http://stdweb.favor2.info`

[5] For example, g-r for Sloan-like filters in order to assess how much the individual photometric system of the image deviates from the catalog one

[6] `www.legacysurvey.org/dr10`

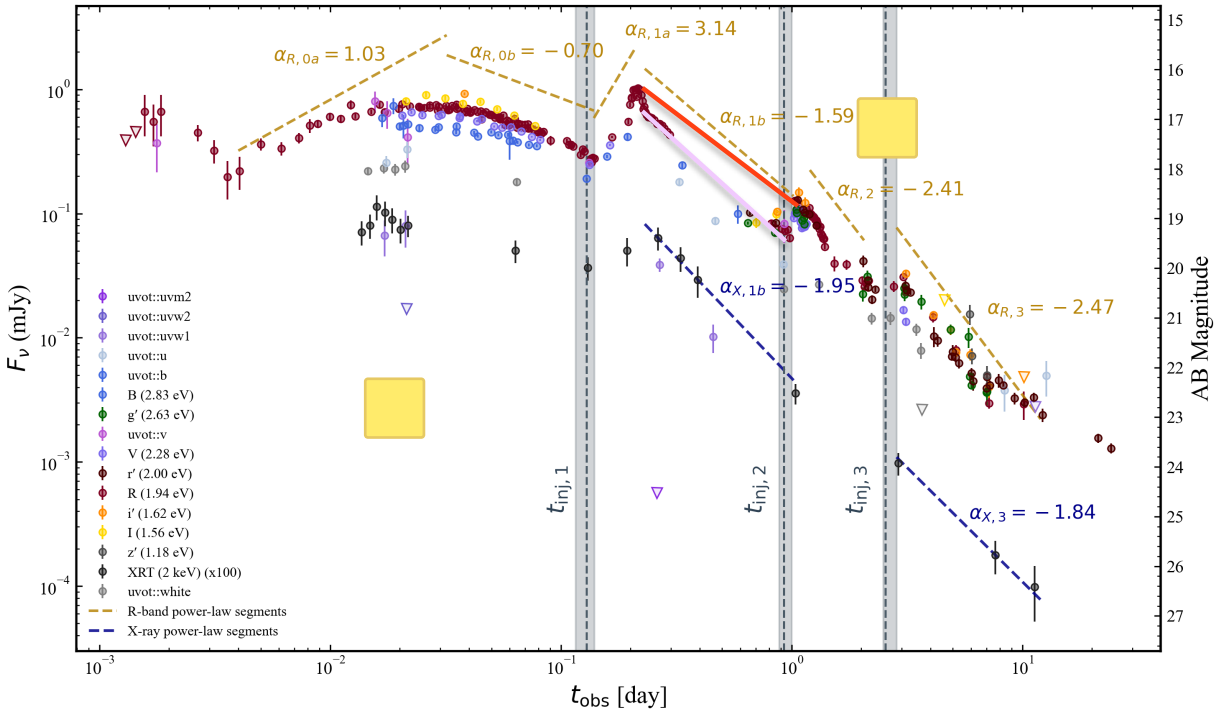

Fig. 5. Observations from this work. Apparent magnitudes corrected for the Milky Way extinction with the calibration of the Milky Way dust maps from (Schlafly & Finkbeiner 2011a). $t_{inj,1}$, $t_{inj,2}$, and $t_{inj,3}$ correspond to the time of the first ($T - T_0 = 0.129^{+0.011}_{-0.013}$), second ($T - T_0 = 0.926^{+0.074}_{-0.042}$), and third ($T - T_0 = 2.55^{+0.301}_{-0.05}$) rebrightenings in days (see Section 4). For clarity, XRT flux densities are scaled by x100 in this plot, and the AB-magnitude axis reflects the corresponding scaled flux densities. The dashed lines represent the power-law fits to the afterglow, and the corresponding temporal slope values are listed in Table 2. The R-band temporal decay fits are shown with a +0.35 dex vertical offset to aid visualization.

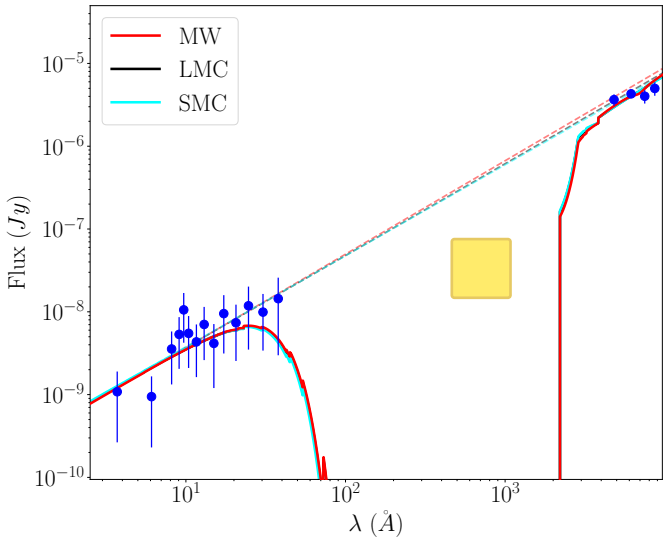

Fig. 6. X-ray-to-optical SED of GRB 250129A at $T - T_0 \sim 7.04$ days using the MW (red), LMC (black), and SMC (cyan) extinction curves. **Dashed lines**: intrinsic simple power law model of the afterglow. **Solid lines**: Best fits to the data, including the X-ray absorption and the optical extinction.

$0.05^{+0.12}_{-0.03}$ mag, $N_{H,X} = 0.89^{+7.39}_{-0.62} \times 10^{+22}\mathrm{cm}^{-2}$ (χ^2_{MW}/d.o.f = 12.12/14). Additionally, the fitted parameters remain consistent across the other extinction curves, with the Large (LMC) and Small Magellanic Clouds (SMC) yielding statistical similar fits of χ^2_{LMC}/d.o.f = 12.45/14 and χ^2_{SMC}/d.o.f = 12.57/14 (see Fig. 6).

In light of these results, we used a no-host dust extinction scenario for the later analyses and did not apply further correction.

3.2. Host Galaxy

We identified two bright possible host galaxies, SDSS 1237655125552333194 (G1) at $z = 0.42$ and SDSS 1237655125552333205 (G2) at $z = 0.26$, with spectroscopic redshifts provided by the Sloan Digital Sky Survey (SDSS) Data Release 12 (DR12) (Ahumada et al. 2020). We also included two faint galaxies identified in the Legacy Survey Catalog: G3 (ra:198.6775,dec:5.0292) and G4 (ra:198.6784, dec: 5.0317) with an estimation of a photometric redshift of $z_{phot} = 0.69$ for G3, and $z_{phot} = 0.64$ for G4, respectively. These f alaxies and their characteristics are presented in table 1 wi redshift (z), magnitude in m_r, the projected angular separation R_0 between the GRB and the galaxy, the offset, and the probabilities of chance alignment $P_{ch}(< R_0)$.

We use Eq. 1–3 from Bloom et al. (2002) and the galaxy number counts from deep optical imaging (Metcalfe et al. 2001; McCracken et al. 2003; Kashikawa et al. 2004), we estimate the probability of finding an unrelated galaxy of magnitude m_r or brighter within the vicinity of GRB 250129A (see Section 3.5 from Becerra et al. 2023):

The P_{ch} is > 20% for G2, G3 and G4, making them unlikely host galaxies. For G1, even though the P_{ch} value is ∼ 2%, its spectroscopic redshift does not match the redshift estimated for GRB 250129A. Therefore, despite the low probability of chance alignment, we also consider it unrelated to our event.

Table 1. Galaxies in the neighborhood of GRB 250129A. Is described for each galaxy: label (see text), redshift (z), magnitude in m_r, the projected angular separation R_0 between the GRB and the galaxy, the offset, and the probabilities of chance alignment $P_{\rm ch}(< R_0)$. The asterisk next to the redshift value for the last two galaxies indicates that it is a photometric redshift.

	z	m_r	R_0 [$''$]	Offset [kpc]	$P_{\rm ch}(< R_0)$
G1	0.42	20.30 ± 0.05	4.48	49.99	2.08
G2	0.26	21.00 ± 0.10	14.82	94.66	29.10
G3	0.69*	23.10	6.85	139.03	36.20
G4	0.64*	22.64	7.85	145.32	32.62

Table 2. Multi-segment temporal (α) and spectral (β) indices of the afterglow. The temporal indices in the R band and X-ray are derived from power-law fits within the time intervals listed in the first column. The onset bump is fitted with a smoothly broken power-law, while single power-law fits are applied to the remaining segments. Spectral indices are obtained from multi-band SED fitting over the corresponding epochs.

Time (days)	Slopes
	Temporal index
0.004-0.032	$\alpha_{\rm R,0a}$ = 1.03±0.05
0.032-0.139	$\alpha_{\rm R,0b}$ = -0.70±0.07
0.139-0.211	$\alpha_{\rm R,1a}$ = 3.14 ±0.40
0.231-1.020	$\alpha_{\rm R,1b}$ = -1.59 ±0.00
1.200-2.060	$\alpha_{\rm R,2}$ = -2.41 ±0.15
2.850-12.000	$\alpha_{\rm R,3}$ = -2.47 ±0.10
0.231-1.020	$\alpha_{\rm X,1b}$= -1.95±0.04
2.850-12.000	$\alpha_{\rm X,3}$ = -1.84 ±0.51
	Spectral index
∼0.08	$\beta_{\rm 0b}$ = -0.75±0.07
∼0.2	$\beta_{\rm 1a}$ = -0.71±0.01
0.30-0.33	$\beta_{\rm 1b}$ = -0.91±0.15
1.2-2.0	β_2 = -1.14±0.79
3.0-4.0	β_3 = -1.25±0.83

4. Interpretation

To model the afterglow emission before the rebrightening episodes seen in the optical and X-rays, we first consider the simple and standard afterglow model of a thin and ultrarelativistic spherical shell. This serves as a good approximation for a uniform top-hat jet viewed on-axis at times before the jet-break time. The shell propagates through the external medium that has number density $n_{\rm ext}(\mathcal{R}) = n_0(\mathcal{R}/\mathcal{R}_0)^{-k} = A\mathcal{R}^{-k}$ with $\mathcal{R}$ the distance from the explosion center, k the index of the density profile, n_0 the density normalization defined at a fixed $\mathcal{R}_0$, and $A = n_0\mathcal{R}_0^k$. It is slowed down as it sweeps up this medium in its path. This gives rise to a two-shock structure, where a forward shock propagates ahead of the shell and shock-heats the swept-up medium, while a reverse shock propagates through the shell, shock-heats it, and extracts its kinetic energy. The shell starts to decelerate when the swept-up mass $M_{\rm sw}(\mathcal{R}) = 4\pi m_p n_{\rm ext}(\mathcal{R})\mathcal{R}^3/(3-k) = M_0/\Gamma_0$, where $M_0 = E_{\rm k,iso}/\Gamma_0 c^2$ and $\Gamma_0 \gg 1$ are the baryon load and coasting bulk Lorentz factor (LF) of the shell, respectively, $E_{\rm k,iso}$ is its isotropic-equivalent kinetic energy after the prompt phase, and m_p and c are the proton mass and speed of light. The corresponding deceleration radius is given by $\mathcal{R}_{\rm dec} = [(3-k)E_{\rm k,iso}/4\pi m_p c^2 A\Gamma_0^2]^{1/(3-k)}$ (e.g. Panaitescu & Kumar 2000), where the bulk of the kinetic energy of the shell is given to the shocked swept-up medium that causes the forward shock afterglow emission to peak. At $\mathcal{R} > \mathcal{R}_{\rm dec}$, the dynamical evolution of the shell follows the Blandford & McKee (1976) solution where its bulk LF declines as a power law in radius with $\Gamma(\mathcal{R}) \propto \mathcal{R}^{-(3-k)/2}$, as dictated by energy conservation.

We model the emission coming from the forward shock using the standard afterglow theory (Sari et al. 1998). The shock accelerates a large fraction of the electrons in the swept up medium into having a power-law energy distribution, with comoving number density $n_e(\gamma) \propto \gamma^{-p}$ for $\gamma > \gamma_m$ and where γ is the LF of the electrons and γ_m is the LF of the minimal energy electrons. These electrons hold a fraction ϵ_e of the total internal energy in the shocked medium, while a fraction ϵ_B goes into generating and/or amplifying small-scale magnetic fields. The accelerated electrons then cool behind the shock front by emitting synchrotron radiation. The power-law temporal index (α) and the spectral index (β) of the afterglow emission ($F_\nu \propto t^\alpha \nu^\beta$) are related through the *closure relations*, where slow-cooling emission produced at a frequency $\nu_m < \nu < \nu_c$ (with ν_m the peak synchrotron frequency of minimal-energy electrons and ν_c the cooling-break frequency (Granot & Sari 2002)) has $\alpha = -3(p-1)/4$ and $\beta = -(p-1)/2$ when $k = 0$. We exploit these relations below to check for consistency and infer the value of p.

4.1. Empirical fitting and probing external shock scenario

Figure 5 shows the optical and X-ray light curves. The optical emission exhibits an onset bump peaking at ∼ 0.03 d, followed by three rebrightening episodes at ∼ 0.2, ∼ 1, and ∼ 2.5 d. The first two rebrightenings are clearly visible, while the third is less pronounced. The X-ray light curve, although sparsely sampled, follows the overall trend of the optical emission; however, the limited data make it difficult to clearly identify distinct rebrightening episodes. To characterize this morphology, we derive the temporal and spectral slopes. The temporal slopes are obtained by fitting power-law functions over the time intervals listed in Table 2. The resulting values are also summarized in that table.

The onset bump has rising and decaying slopes of 1.03 ± 0.05 and -0.70 ± 0.07, respectively. Assuming a constant-density ISM, a slow-cooling synchrotron regime, and no energy injection in this phase, we infer an electron power-law index of $p = 1.93 \pm 0.09$. This is somewhat smaller than typically reported for GRBs (e.g., Kumar & Zhang 2015). However, we measure a spectral index of 0.65 ± 0.02 at 0.06 d, which, under the slow-cooling assumption, implies $p = 2.3 \pm 0.04$. This value is consistent with the commonly observed range (Kumar & Zhang 2015).

The discrepancy between the values of p inferred from the temporal decay versus the spectrum likely stems from the short duration of the first decay phase. Measuring a slope over such a limited interval near the peak is prone to curvature effects, leading to an artificially shallow decay measurement. Indeed, the fits obtained with the NMMA/AFTERGLOWPY code (Section 4.2) are consistent with the assumed physical scenario without requiring early energy injection during the onset bump (i.e., before the first reebrightening). We therefore attribute the low temporal p-value to uncertainties in the slope measurement rather than intrinsic physics.

The first rebrightening after the onset bump rises with a temporal slope of 3.14 ± 0.40, after which it declines with a slope of -1.59. The second and third rebrightening episodes are followed by more rapid declines of -2.41 ± 0.15 and -2.47 ± 0.10. This steepening is indicative of a jet break. Due to limited data, we are unable to calculate the rising slopes of the second and third rebrightening episodes.

The spectral indices measured at about 0.08, 0.2, 0.3, 1.2-2, and 7 days after the trigger are -0.75 ± 0.07, -0.71 ± 0.01, $-0.91 \pm$

0.15, −1.14±0.79 , and −1.25±0.83 (cf. Table 2). The steepening of the spectral index at late times suggests the passage of the cooling frequency, while the steep late-time temporal decays are consistent with a jet break scenario.

4.2. Agnostic approach

Framework and analysis period We aim to extract the physical parameters of the jet and emission properties by analyzing the light curve data with the AFTERGLOPWY model (Ryan et al. 2020) using the Bayesian inference framework NMMA (Pang et al. 2023). The AFTERGLOWPY package models the GRB afterglow as the result of synchrotron emission from accelerated electrons. Here we make the explicit assumption that the jet propagates inside a constant density interstellar medium (ISM) with $n_{\rm ext} = n_{\rm ISM}$. The jet structure is assumed as a top-hat jet for which the isotropic-equivalent kinetic energy, $E_{\rm k,iso}$, is constant across the jet aperture with half-opening angle $\theta_{\rm j}$. Moreover, the dynamical evolution of the jet in AFTERGLOWPY does not consider a coasting phase and instead makes the simplifying assumption that it has already decelerated and follows the asymptotic power-law decline of its bulk Lorentz factor with radius. For this reason, when analyzing the data from GRB 250129A with AFTERGLOWPY, we exclude early data within the first 0.05 days (4320 s) post-burst, as these data points show a rising light curve that is likely due to a jet coasting phase and can not be properly modeled in AFTERGLOWPY.

Energy injections in a phenomenological approach In order to capture the rebrightening epochs from GRB 250129A's afterglow, we set an ad-hoc prescription that allows the jet energy to vary with time. Specifically, we introduce an energy injection parameter $\Delta \log_{10} E$ that, starting from time $t_{\rm inj}$, linearly increases the jet energy within a given time interval (see Appendix E for further details and explanation regarding the energy injection computation within NMMA). Naturally, this parametrization can be extended to include multiple energy injections. We emphasize that this prescription represents a phenomenological approach and does not account for the mechanism underlying the increase in jet energy nor its exact temporal dependence. Despite the limitations in our modeling prescriptions, the ad hoc increase of the jet energy still allows us to phenomenologically recover the rebrightening in the afterglow light curve and statistically investigate the number of rebrightenings and their approximate duration.

To infer the posterior $p(\vec{\theta}|d)$ from the light curve data d, we sample the parameter space of the model using the nested sampling algorithm as implemented in PYMULTINEST (Feroz et al. 2009; Buchner et al. 2014). In particular, we use the likelihood function $\ln \mathcal{L}(\vec{\theta}|d)$, which compares the observed magnitudes to the model predictions from AFTERGLOWPY. The model parameters and priors are listed in Table 3. In addition to the model parameters, NMMA also samples a nuisance parameter $\sigma_{\rm sys}$ that accounts for systematic uncertainty in the modeling. Throughout the analysis, we fix the redshift at $z = 2.151$ (Sec. 1), corresponding to a luminosity distance of $d_L = 17.3$ Gpc. We begin by establishing a reference baseline to evaluate the statistical significance of the observed rebrightening epochs. Specifically, we select data from the time interval between 0.05 and 0.2 days, which we refer to as the "early time" dataset. The posterior light curves estimated using the data from this interval serve as a proxy for a standard GRB afterglow in our subsequent analysis (see Table 3). Using posterior light curves derived from the "early time" data, we compute the average chi-squared statistic, $\langle \chi^2_j \rangle$, for each data point (see Appendix E for details). In the R band, the computed $\langle \chi^2_j \rangle$ values reveal three distinct rebrightening phases spanning the intervals [0.15, 1] days, [1, 3] days, and [3, 30] days (see Figure 5). To investigate these features, we apply the ad hoc energy injection model described in Eq. (E.1) (see Appendix E for details) and analyze the full dataset beyond 0.05 days. Parameter priors are listed in Tab. 3.

In total, four models are considered, namely, one without energy injection, ones with 1, 2 and 3 energy injection epochs. The posterior distributions for the four models considered are summarized in Tab. 4 and visualized in Fig. 7. As described in Pang et al. (2023), the parameter $\sigma_{\rm sys}$ is included to account for the systematic uncertainty within the lightcurves modeling. Comparing the inferred systematic uncertainty across models with varying numbers of energy injection epochs to the baseline model without injections, we observe a general decreasing trend. This suggests that including energy injections improves the model's ability to fit the data.

We also compare the maximum likelihood values and compute the Bayes factors between the models, as reported in Tab. 4. Our analysis shows that models with one, two, or three injection epochs yield higher maximum likelihoods and are favored by the Bayes factor. However, in the case of three injections, the (ln-) Bayes factor ($\ln \mathcal{B} \sim 6$) relative to the two-injection model is modest. Furthermore, the estimated fractional energy injected associated with the third injection is notably small. This is consistent with the best-fit light curves, as there is minimal difference between the 2-injection and 3-injection light curves shown in Fig. 8, leading us to conclude that only the first two rebrightenings are statistically significant. This conclusion is further supported by visual inspection of the light curve (cf. Fig. 5): the first and second rebrightenings a arly identifiable, whereas the third episode is less distinct.

Despite the apparent consistency between the model and data for each individual rebrightening phase when energy injection is included, the inferred physical parameters, e.g., the electron distribution power-law index p, vary significantly across th ferent epochs. Energy injection provides a physically moti explanation for afterglow rebrightenings. One possible interpretation is the refreshed-shock scenario, in which the ejecta possess a distribution of Lorentz factors rather than a single characteristic value. As the forward shock decelerates, slower but energetically significant ejecta catch up with the bl wave and re-energize it, leading to a rebrightening of the aft w light curve (Sari & Mészáros 2000). This framework is a adopted by Laskar et al. (2015b), who model energy injection as arising from a continuous distribution of Lorentz factors released over a time interval short compared to the afterglow timescale. The variation between the inferred parameters for GRB 250129A indicates that such energy injection alone is insufficient to capture the underlying physics in a self-consistent manner.

Although the energy injection scenario could in principle explain the rebrightening, it is challenging to fully interpret the observed temporal and spectral changes before and after the injection process, suggesting a detailed treatment of the underlying physics as done in the next section.

4.3. Refreshed Shocks scenario: Shell Collisions

The multiple pulses in the prompt emission phase suggest that there are multiple mass shells launched by the central engine. We consider that the earliest launched shell (outermost in the radial direction, or the external shock) has a bulk Lorentz factor (LF)

Table 3. Parameters employed and the associated prior bound in our Bayesian inferences. Three sets of priors are used for each of the re-brightening peaks.

Parameter	Prior bound
($\log_{10}$-) On-axis isotropic equivalent energy $E_{\rm k,iso}$ [erg]	$[47, 57]$
($\log_{10}$-) Ambient medium's density $n_{\rm ISM}$ [cm^{-3}]	$[-6, 2]$
($\log_{10}$-) Energy fraction in electrons $\epsilon_{\rm e}$	$[-4, 0]$
($\log_{10}$-) Energy fraction in magnetic field $\epsilon_{\rm B}$	$[-8, 0]$
Electron distribution power-law index p	$[2.01, 3]$
Viewing angle [degree]	$[0, 36]$
Jet core opening angle $\theta_{\rm j}$ [degree]	$[0.6, 20]$
Systematic error $\sigma_{\rm sys}$ [mag]	$[0, 2]$
Start time of energy injection $t_{\rm inj}$ [day]	$[0.07, 0.3]$, $[0.7, 1.3]$, $[2.5, 3.5]$
Duration of energy injection $\Delta t_{\rm inj}$ [day]	$[0.001, 0.3]$, $[0.001, 0.4]$, $[0.001, 1]$
($\log_{10}$-) Fractional energy injected $\Delta \log E_{\rm k,iso}$	$[0, 3]$, $[0, 4]$, $[0, 4]$

Table 4. Parameters employed in our Bayesian inferences. We report maximum likelihood values at 95% credibility for various sub-datasets considered.

Parameter	No injection	1-injection	2-injection	3-injection
($\log_{10}$-) On-axis isotropic equivalent energy $E_{\rm k,iso}$ [erg]	$52.53^{+0.43}_{-0.02}$	$53.72^{+0.95}_{-0.58}$	$53.85^{+0.80}_{-0.18}$	$54.12^{+0.93}_{-0.36}$
($\log_{10}$-) Ambient medium's density $n_{\rm ISM}$ [cm^{-3}]	$-0.31^{+2.3}_{-0.22}$	$-0.32^{+2.32}_{-3.45}$	$0.82^{+0.81}_{-3.8}$	$-0.84^{+1.53}_{-4.65}$
($\log_{10}$-) Energy fraction in electrons $\epsilon_{\rm e}$	$-0.01^{+-0.0}_{-0.44}$	$-0.93^{+0.45}_{-0.84}$	$-0.61^{+0.14}_{-0.81}$	$-0.89^{+0.29}_{-0.96}$
($\log_{10}$-) Energy fraction in magnetic field $\epsilon_{\rm B}$	$-1.86^{+1.66}_{-0.35}$	$-3.71^{+2.21}_{-1.23}$	$-5.26^{+2.31}_{-0.48}$	$-4.25^{+2.78}_{-0.9}$
Electron distribution power-law index p	$2.29^{+0.09}_{-0.06}$	$2.68^{+0.09}_{-0.12}$	$3.00^{+0.00}_{-0.03}$	$3.00^{+0.00}_{-0.06}$
Viewing angle [degree]	$7.15^{+8.85}_{-0.5}$	$13.44^{+3.99}_{-9.94}$	$0.13^{+9.61}_{-0.13}$	$14.79^{+4.38}_{-10.59}$
Jet core opening angle $\theta_{\rm j}$ [degree]	$9.75^{+10.25}_{-0.2}$	$16.62^{+3.38}_{-10.76}$	$16.66^{+3.34}_{-5.88}$	$15.93^{+4.07}_{-10.92}$
Time of 1$^{\rm st}$ energy injection $t_{\rm inj,1}$ [day]	-	$0.128^{+0.021}_{-0.015}$	$0.126^{+0.012}_{-0.015}$	$0.129^{+0.011}_{-0.013}$
Duration of 1$^{\rm st}$ energy injection $\Delta t_{\rm inj,1}$ [day]	-	$0.070^{+0.024}_{-0.033}$	$0.075^{+0.019}_{-0.021}$	$0.075^{+0.014}_{-0.018}$
($\log_{10}$-) 1$^{\rm st}$ Fractional energy injected $\Delta \log E_1$	-	$0.51^{+0.057}_{-0.065}$	$0.512^{+0.059}_{-0.039}$	$0.515^{+0.059}_{-0.033}$
Time of 2$^{\rm nd}$ energy injection $t_{\rm inj,2}$ [day]	-	-	$0.974^{+0.031}_{-0.077}$	$0.926^{+0.074}_{-0.042}$
Duration of 2$^{\rm nd}$ energy injection $\Delta t_{\rm inj,2}$ [day]	-	-	$0.007^{+0.102}_{-0.006}$	$0.083^{+0.037}_{-0.082}$
($\log_{10}$-) 2$^{\rm nd}$ Fractional energy injected $\Delta \log E_2$	-	-	$0.166^{+0.008}_{-0.043}$	$0.204^{+0.013}_{-0.034}$
Time of 3$^{\rm rd}$ energy injection $t_{\rm inj,3}$ [day]	-	-	-	$2.55^{+0.301}_{-0.05}$
Duration of 3$^{\rm rd}$ energy injection $\Delta t_{\rm inj,3}$ [day]	-	-	-	$0.282^{+0.294}_{-0.281}$
($\log_{10}$-) 3$^{\rm rd}$ Fractional energy injected $\Delta \log E_3$	-	-	-	$0.053^{+0.02}_{-0.044}$
Systematic error $\sigma_{\rm sys}$ [mag]	$0.38^{+0.03}_{-0.04}$	$0.24^{+0.03}_{-0.02}$	$0.19^{+0.03}_{-0.01}$	$0.17^{+0.03}_{-0.01}$
(ln-) likelihood ratio $\ln \Lambda$	reference	87.17	128.52	144.15
(ln-) Bayes factor $\ln \mathcal{B}$	reference	78.88 ± 0.22	110.44 ± 0.24	116.95 ± 0.25

of $\Gamma_{0,1} \gg 1$, which starts to decelerate at $\mathcal{R} \geq \mathcal{R}_{\rm dec}$. Later shells ejected with bulk LFs $\Gamma_{0,i} \gg 1$, with $i = (2, 3, 4)$, propagate almost unimpeded and may collide with the outer shell in succession, thereby dissipating their kinetic energy and causing potential rebrightening episodes (e.g. Kumar & Piran 2000; Sari & Mészáros 2000; Zhang & Mészáros 2002). The correspondence between the prompt pulses and shells, and the timing analyses on the temporal features, are crucial to identify whether collisions could occur, which has been applied in the explanation of GRB 140304A (Laskar et al. 2018), GRB 240529A (Sun et al. 2024), GRB 060729 (Geng et al. 2025b), and GRB 250221A (Angulo-Valdez et al. 2025) recently. When the two shells collide, another set of forward and reverse shocks develops, where the FS heats the already relativistically hot material of the outer shell, while the RS heats the inner shell.

The first optical rebrightening episode starts at $T_1 \simeq 1.1 \times 10^4$ s. Since the rebrightening occurs after the peak of the light curve, it is clear that the outermost shell has already decelerated. In general, for an ultrarelativistic shell with dynamics $\Gamma^2 \propto \mathcal{R}^{-m}$, where $m = 0$ for a coasting shell at $\mathcal{R} < \mathcal{R}_{\rm dec}$ and $m = 3 - k$ for a decelerating shell with self-similar evolution at $\mathcal{R} > \mathcal{R}_{\rm dec}$, the on-axis arrival time of radiation is $T_z \equiv T/(1+z) \simeq \mathcal{R}/2(1+m)\Gamma^2 c$. Then, given $\hat{T}_1 \equiv T_1/T_{\rm dec}$ ($T_{\rm dec} \simeq 2 \times 10^3$ s if we treat the peak time of the first onset bump as the deceleration time), we can calculate the radius at which shocks develop in the two colliding shells, such that (e.g., Laskar et al. 2018; Angulo-Valdez et al. 2025)

$$\hat{\mathcal{R}}_1 \equiv \frac{\mathcal{R}_1}{\mathcal{R}_{\rm dec}} = [(4-k)\hat{T}_1]^{1/(4-k)} \simeq 2.2 \quad (k = 0)\,, \tag{1}$$

with the assumption that the material that makes the dominant contribution to the re-brightened emission is moving with LF $\sim \Gamma_1$. To reach radius $\mathcal{R}_1$, the outer shell takes lab-frame time of $t_1 = t_{\rm em,1} + \mathcal{R}_1/c + (\hat{\mathcal{R}}_1^{4-k} - 1)T_{\rm dec,z}/(4-k)$, where $t_{\rm em,i}$ marks the launching time of the i-th shell. To reach the same radius, the inner shell takes lab-frame time $t_1 = t_{\rm em,2} + \mathcal{R}_1/\beta_{0,2}c \simeq t_{\rm em,1} + \delta t_{\rm em,12} + (1 + 1/2\Gamma_{0,2}^2)\mathcal{R}_1/c$, where $t_{\rm em,1} < t_{\rm em,2} < T_{90}/(1+z) \approx 83$ s and $\delta t_{\rm em,12}$ is the waiting time between the ejection of the first two mass shells. Since $\delta t_{\rm em,12}(1+z)/T_{\rm dec} \ll 1$, it can be neglected when equating the lab-frame arrival times of the two shells at $\mathcal{R}_1$, which yields an estimate of the contrast between the initial LFs

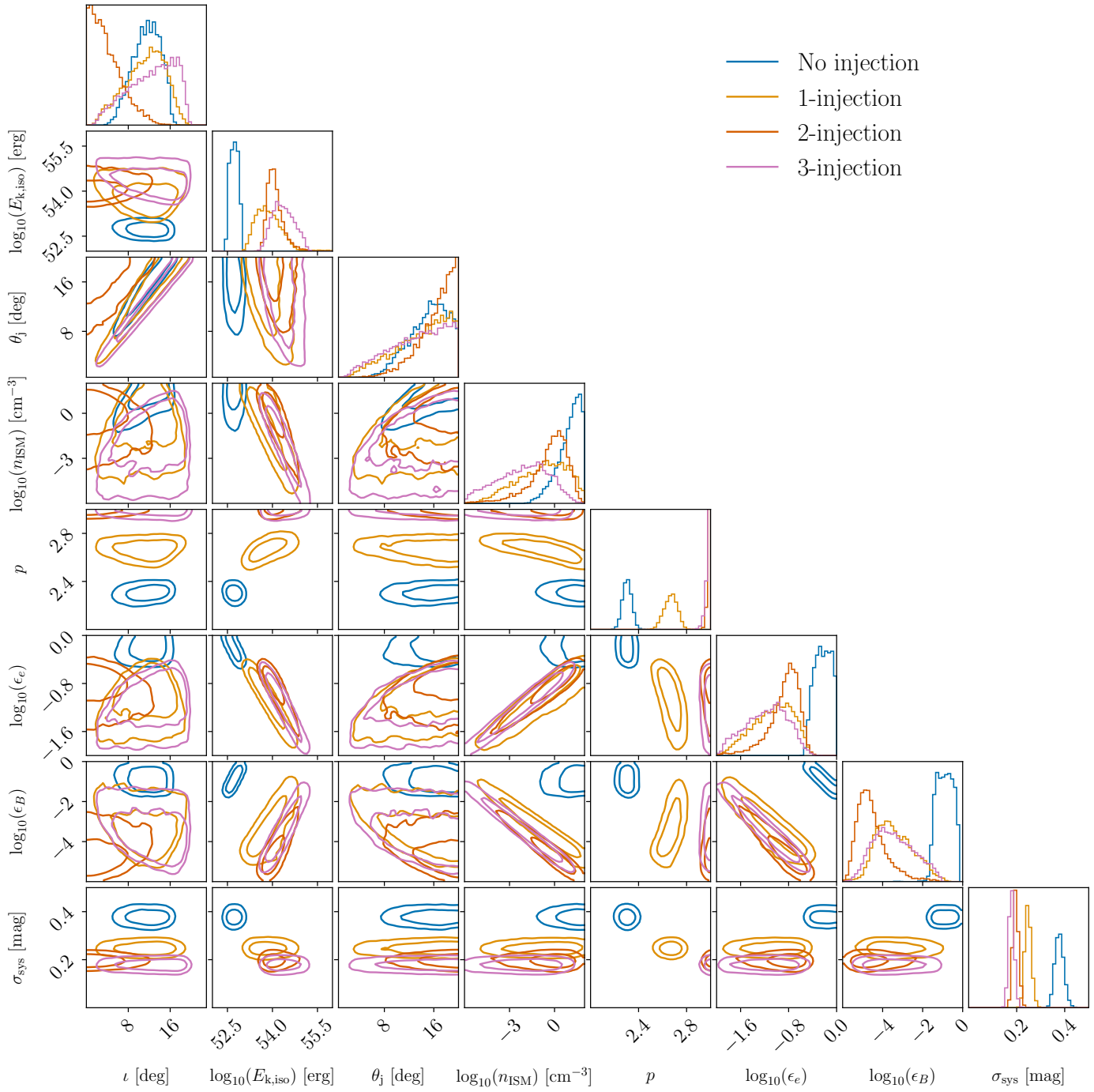

Fig. 7. Posterior of the GRB afterglow for each of the models (see section 4.2) considered using NMMA. Priors are given in Table 3. The different times on rebrightening (e.g., energy injections) are consistent with the light curve (see Figure 5).

of the two shells,

$$\frac{\Gamma_{0,1}}{\Gamma_{0,2}} \approx \sqrt{\frac{\hat{\mathcal{R}}_1^{4-k}-1}{(4-k)\hat{\mathcal{R}}_1}} \approx \frac{[(4-k)\hat{T}_1]^{\frac{(3-k)}{2(4-k)}}}{\sqrt{4-k}} \simeq 1.6 \quad (k=0)\,, \quad (2)$$

where the second approximation assumes that $\hat{\mathcal{R}}_1 \gg 1$. During the collision, the bulk Lorentz factor of the FS can be approximated as the velocity of the merged two shells (e.g., Piran 1999b)

$$\Gamma_{\rm F} \simeq \left(\frac{\Gamma_1 m_1 + \Gamma_{0,2} m_2}{m_1/\Gamma_1 + m_2/\Gamma_{0,2}}\right)^{1/2} \in [\Gamma_1, \Gamma_{0,2}], \quad (3)$$

according to the conservation of energy and momentum, where m_1 and m_2 are the masses of the two shells, respectively. The co-moving thickness of the leading shell can be approximated as $\Delta_1 \simeq \eta\mathcal{R}_1/\Gamma_1 \simeq 2\eta\Gamma_{0,2}^2 cT_{1,z}/\Gamma_1$ at T_1, where η is a geometry factor that could be taken as $\eta = 1/4(3-k)$ from the consideration of particle number conservation for a homogeneous shell. Let $\beta_{\rm F1}$ denote the relative velocity between the forward shock and the leading shell. We may expect that the optical flare would reach its peak luminosity when the FS has crossed the entire leading

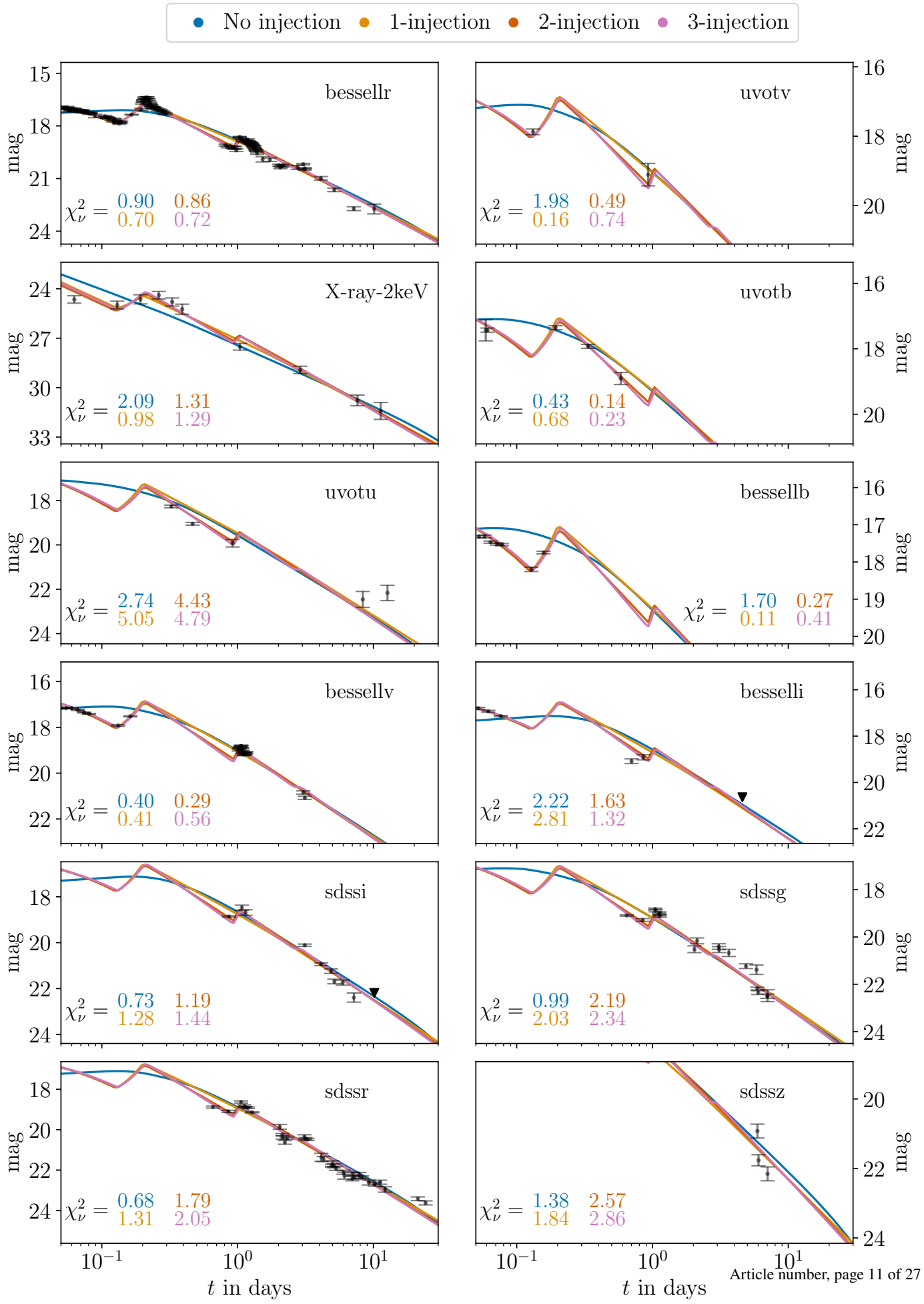

Fig. 8. Best-fit light curves of the GRB afterglow, together with the reduced χ^2 of each filter, for each of the models considered.

Table 5. Parameters employed in the afterglow fitting within the framework of multiple shell collisions.

Parameters	First Shell	Second Shell	Third Shell	First Collision			Second Collision		
				FS	RS	ES	FS	RS	ES
$E_{\rm k,iso}$ (10^{53} erg)	$1.70^{+0.12}_{-0.11}$	10.0	8.0						
Γ_0	$97.72^{+2.28}_{-4.40}$	39.0	24.5						
$\theta_{\rm j}$ (rad)	$0.10^{+0.02}_{-0.02}$								
$n_{\rm ISM}$ (cm^{-3})	$1.05^{+0.27}_{-0.16}$								
$\epsilon_{\rm e}$	$0.09^{+0.01}_{-0.00}$			0.18	0.10	0.11	0.10	0.10	0.12
$\epsilon_{\rm B}$ (10^{-3})	$2.51^{+0.31}_{-0.32}$			10.0	10.0	2.0	10.0	10.0	2.0
p	$2.07^{+0.00}_{-0.00}$			2.3	2.3	2.3	2.3	2.3	2.4
η	0.12	0.12							

shell after an observational duration of (Geng et al. 2025b)

$$
\begin{aligned}
T_{\rm flare,1} - T_1 &\simeq (1+z)\Gamma_{\rm F}(1-\beta_{\rm F}\cos(\min[\theta_{\rm j}, 1/\Gamma_{\rm F}]))\frac{\Delta_1}{\beta_{\rm F1}c} \quad (4)\\
&\simeq 2\eta\Gamma_{0,2}^2/(\Gamma_{\rm F}\Gamma_1\beta_{\rm F1})T_1\\
&\in [\frac{\Gamma_{0,2}}{\Gamma_{0,1}}\hat{\mathcal{R}}_1^{(3-k)/2}, \frac{\Gamma_{0,2}^2}{\Gamma_{0,1}^2}\hat{\mathcal{R}}_1^{3-k}]\frac{2\eta}{\beta_{\rm F1}}T_1
\end{aligned}
$$

for $\theta_j > 1/\Gamma_{\rm F}$, where the last range is obtained by taking the two extremes for $\Gamma_{\rm F}$ in Equation (3). As observation of the R band data gives a dimensionless timescale of $\delta\hat{t} = (T_{\rm flare,1} - T_1)/T_1 \simeq 0.5$ for the rising phase of the first optical flare, Equations (1 - 4) suggest that $\eta \leq 0.12$ since $\beta_{\rm F1} < 1$.

The analyses on the shock dynamics above show the conditions for the shell collision. We further conduct more accurate numerical calculations to verify that this scenario can well explain the multiple peaks in GRB 250129A with a set of reasonable parameters. Before collision, the dynamic of the external shock of the first outflow is described by a generic model based on energy conservation (Huang et al. 1999; Pe'er 2012). During collision, the dynamics of the FS/RS system is described by the mechanical model that incorporates the conservation of energy and momentum (Beloborodov & Uhm 2006; Geng et al. 2025a). We calculate the time-dependent electron spectrum heated by each shock by solving the continuity equation in energy space (Geng et al. 2018), and derive the resulting synchrotron and synchrotron self-Compton emission using standard formulae (Rybicki & Lightman 1979). In our calculations, the environment is assumed to be ISM-type for simplicity, and the accelerated post-shock electron spectrum is generalized as a Maxwellian component and a power-law component for each shocked/emitting region. This hybrid spectrum is characterized by an energy fraction parameter defined as the nonthermal energy fraction of the total, and we set it to a typical value of ~ 0.4 following earlier studies for simplification (Giannios & Spitkovsky 2009; Gao et al. 2024). We fit the early afterglow within 10^4 s, produced by the outermost shell, using the standard Bayesian approach to derive its parameters: $E_{\rm k,iso}$, $\Gamma_{0,1}$, $\theta_{\rm j}$, $n_{\rm ISM}$, $\epsilon_{\rm e}$, ϵ_B, and p. We assume that subsequently launched shells share the same jet opening angle $\theta_{\rm j}$ and circumburst density $n_{\rm ISM}$ as the outermost shell. To account for the observed optical flares, we introduce two additional shells that are launched after the outermost shell. Since their initial bulk Lorentz factors are only of order several tens, deceleration is not yet significant; these shells therefore move at nearly constant speed until they catch up and collide with the preceding outermost shell, producing the optical flares. During each collision, the equation of state of the material ahead of the FS is determined by calculating the averaged Lorentz factor of material accumulated by the leading shock with adiabatic cooling accounted (e.g., Nava et al. 2013). The parameters of the subsequent two shells and the relevant collisions are chosen according to the discussions above (e.g., p in Sec. 4.1) and several trials around typical values (cf. Table 5).

As shown in Fig. 9, the multi-wavelength afterglow and two significant rebrightenings could be well fitted with a set of parameters listed in Tab. 5. For the first collision that generates the intense optical flare, the adopted $\Gamma_{0,1} \simeq 100$ and $\Gamma_{0,2} \simeq 40$ generally align with Equation 2. The optical flare is mainly contributed by the FS as the FS sweeps and re-accelerates the material collected from the environment by the leading shell. After each collision, the FS crosses the entire leading shell, and the merged shell evolves into a new leading/outmost external shock propagating in the environment. The shell collision scenario provides details of the shock interaction in comparison with the traditional energy injection scenario, while the fitting results of both scenarios are consistent with each other.

5. Conclusion and discussion

We explored whether the light curve of GRB 250129A can be reproduced a physically consistent set of microphysical parameters commonly adopted in the literature, and a sequence of refreshed shocks produced by collisions between shells with different bulk Lorentz factors ejected during the prompt emission phase (see sec 4.3). To this end, we adopted a kinematic approach to calculate the dynamical evolution and radiation from such shell collisions, using a numerical code that will be publicly released by Geng et al. (in preparation).

While the present analysis requires the introduction of additional microphysical parameters to describe the separate emission components and does not involve a full Bayesian inference, the observed flares can be broadly reproduced using a reasonable set of plausible shell parameters and typical microphysical parameters ($\epsilon_{\rm e} \simeq 0.1$, $\epsilon_B \simeq 10^{-3}$–$10^{-2}$). This supports the physical plausibility of the refreshed-shock interpretation. While the present analysis demonstrates the physical plausibility of the refreshed-shock scenario using standard parameter values, fu-

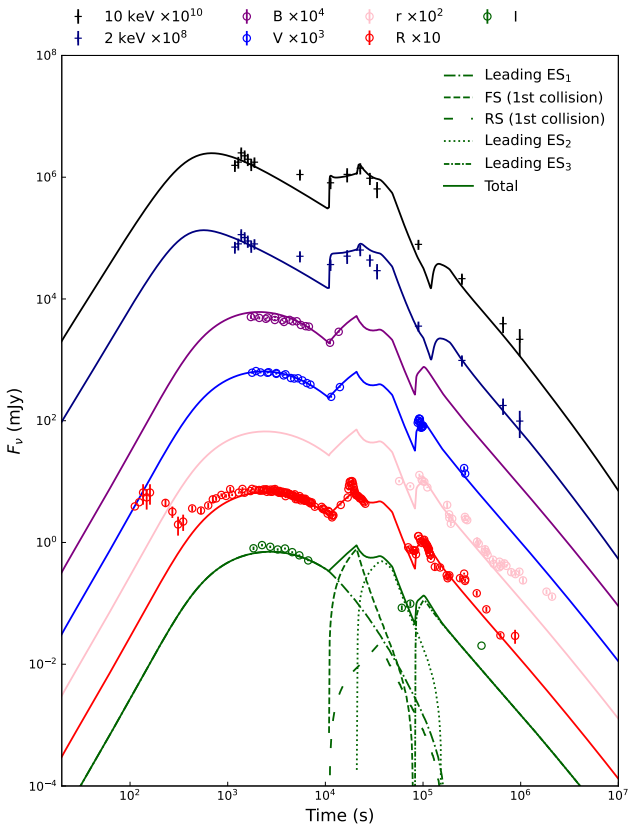

Fig. 9. Fit to the GRB afterglow within the scenario of shock collision. The dash-dotted line is the emission of the outermost external shock (marked as ES_1) propagating in the environment for the first outflow. The dashed and loosely dashed line represents emission from the forward shock (FS) and the reverse shock (RS) during the collision, respectively. The dotted line is the emission of the external shock at the second stage (marked as ES_2) after the FS crossing the leading shell, which is refreshed again to and marked as ES_3 at the third stage (densely dashed-dotted lines) by the second collision near 1 day. Since the crossing timescales of the FS/RS during the second collision are relatively shorter and their flux contribution are sub-dominant, they are not shown by individual lines for clarity. The total flux from all emission components is given by the solid line for each band.

ture studies combining informative priors from particle-in-cell simulations with broader multi-wavelength coverage (e.g., radio and GeV bands) could provide tighter constraints on the system parameters.

Several lines of evidence support the refreshed-shock scenario considered here. First, the prompt emission of GRB 250129A displayed four distinct emission episodes in gamma-rays and at least one in optical, suggesting the ejection of multiple relativistic shells. Second, the optical rebrightenings exhibit a steep temporal index, in contrast to the shallower behaviors seen in some GRBs (Filgas et al. 2011; Nardini et al. 2014) at a comparable epochs ($\sim 10^4$ s). Such steepness supports the interpretation that these are new emission components associated with shell collisions, rather than by gradual energy injection process arising from a continuous Lorentz-factor stratification or prolonged central-engine activity. The latter scenario is difficult to reconcile with the data, as it remains unclear how a central engine—whether a magnetar or an accreting black hole—could directly modulate the blast-wave energetics at such large radii. If multiple jets arise from accretion onto the central compact object, the properties of these shells (e.g., velocities, kinetic energies) could provide valuable insights into the system's accretion history and jet-launching mechanisms. However, the kinetic energy of the rear shells may not be well constrained due to the lack of simultaneous, high-quality X-ray data and the degeneracy of microphysical parameters during the collision.

An alternative explanation not explored in detail in this work involves variations in the external density profile encountered by the relativistic blast wave. Such density structures are plausible in the vicinity of massive progenitors, where strong stellar winds and eruptive mass-loss episodes can shape a complex circumburst environment (Ramirez-Ruiz et al. 2001). However, previous studies indicate that even substantial density jumps are generally insufficient to reproduce sharp and intense optical flares such as the one observed at $\sim 10^4$ s in GRB 250129A (Nakar & Granot 2007; van Eerten et al. 2009; Gat et al. 2013; Geng et al. 2014). Similarly, off-axis viewing scenarios are disfavored, as they generally predict a smooth evolution and cannot support a sequence of multiple, rapidly rising rebrightening episodes (Beniamini et al. 2020; Abdikamalov & Beniamini 2025; Wang et al. 2025). As observational coverage continues to improve in a timely manner, the detection of more GRBs exhibiting similar behavior could provide deeper insight into the prolonged activity and complex dynamics of GRB central engines.

Data Availability

The raw measurements are all public and can be retrieved atthe GRB 250129A SkyPortal Public Page. The images are available upon request.

References

Abbott B. P., et al., 2017, ApJ, 850, L40
Abdikamalov E., Beniamini P., 2025, MNRAS, 539, 2707
Ahumada R., et al., 2020, ApJS, 249, 3
Akl D., et al., 2025a, GRB Coordinates Network, 39106, 1
Akl D., et al., 2025b, GRB Coordinates Network, 39246, 1
Albin E., 2018, 231, 444
Angulo-Valdez C., et al., 2025, arXiv e-prints, p. arXiv:2510.19132
Antier S., et al., 2020, MNRAS, 492, 3904
Antier S., et al., 2025, GRB Coordinates Network, 39096, 1
Azzam Y. A., Ali G. B., Ismail H. A., Haroon A., Selim I., 2010, in Haubold H. J., Mathai A., eds, Proceedings of the Third UN/ESA/NASA Workshop on the International Heliophysical Year 2007 and Basic Space Science. Springer Berlin Heidelberg, Berlin, Heidelberg, pp 175–187
Azzam Y. A., et al., 2022, Experimental Astronomy, 53, 45
Basa S., et al., 2022, in Marshall H. K., Spyromilio J., Usuda T., eds, Society of Photo-Optical Instrumentation Engineers (SPIE) Conference Series Vol. 12182, Ground-based and Airborne Telescopes IX. p. 121821S, doi:10.1117/12.2627139
Beardmore A. P., Dichiara S., Page K. L., Neil Gehrels Swift Observatory Team 2025, GRB Coordinates Network, 39066, 1
Becerra R. L., et al., 2023, MNRAS, 522, 5204
Becker A., 2015, HOTPANTS: High Order Transform of PSF ANd Template Subtraction, Astrophysics Source Code Library, record ascl:1504.004
Beloborodov A. M., Uhm Z. L., 2006, ApJ, 651, L1
Beniamini P., Granot J., Gill R., 2020, MNRAS, 493, 3521
Bertin E., 2010, SWarp: Resampling and Co-adding FITS Images Together, Astrophysics Source Code Library, record ascl:1010.068 (ascl:1010.068)
Blandford R. D., McKee C. F., 1976, Physics of Fluids, 19, 1130
Bloom J. S., Frail D. A., Sari R., 2001, AJ, 121, 2879
Bloom J. S., Kulkarni S. R., Djorgovski S. G., 2002, AJ, 123, 1111
Bochenek A., Perley D. A., 2025, GRB Coordinates Network, 39099, 1
Buchner J., et al., 2014, Astron. Astrophys., 564, A125
Burdanov A. Y., et al., 2022, PASP, 134, 105001
Busmann M., et al., 2025, A&A, 701, A225
Cano Z., Wang S.-Q., Dai Z.-G., Wu X.-F., 2017, Advances in Astronomy, 2017, 8929054
Chambers K. C., et al., 2016, arXiv e-prints, p. arXiv:1612.05560
Dai Z. G., Lu T., 1998, A&A, 333, L87

Dai Z. G., Lu T., 2002, Astrophys. J. Lett., 565, L87
Delrez L., et al., 2018, preprint, (arXiv:1806.11205)
Demory B. O., et al., 2020, A&A, 642, A49
Dutton D. A., Reichart D. E., Haislip J. B., Kouprianov V. V., Shaban O. H., Soto A. V., 2022, Publications of the Astronomical Society of the Pacific, 134, 015001
Eichler D., Livio M., Piran T., Schramm D. N., 1989, Nature, 340, 126
Evans P. A., et al., 2007, Astronomy & Astrophysics, 469, 379
Evans P. A., et al., 2009, MNRAS, 397, 1177
Feroz F., Hobson M. P., Bridges M., 2009, Mon. Not. Roy. Astron. Soc., 398, 1601
Filgas R., et al., 2011, A&A, 526, A113
Filippenko A. V., Li W. D., Treffers R. R., Modjaz M., 2001, in Paczynski B., Chen W.-P., Lemme C., eds, Astronomical Society of the Pacific Conference Series Vol. 246, IAU Colloq. 183: Small Telescope Astronomy on Global Scales. p. 121
Fraija N., Betancourt Kamenetskaia B., Galvan-Gamez A., Dainotti M. G., Becerra R. L., Dichiara S., Veres P., do E. S. Pedreira A. C. C., 2022, Astrophys. J., 933, 243
Frederiks D., Lysenko A., Ridnaya A., Svinkin D., Tsvetkova A., Ulanov M., Cline T., Konus-Wind Team 2025, GRB Coordinates Network, 39116, 1
Gaia Collaboration et al., 2023, A&A, 674, A33
Gao H.-X., Geng J.-J., Sun T.-R., Li L., Huang Y.-F., Wu X.-F., 2024, ApJ, 971, 81
Gat I., van Eerten H., MacFadyen A., 2013, ApJ, 773, 2
Geng J. J., Wu X. F., Li L., Huang Y. F., Dai Z. G., 2014, ApJ, 792, 31
Geng J. J., Wu X. F., Huang Y. F., Li L., Dai Z. G., 2016, ApJ, 825, 107
Geng J.-J., Huang Y.-F., Wu X.-F., Zhang B., Zong H.-S., 2018, ApJS, 234, 3
Geng J.-J., et al., 2025a, arXiv e-prints, p. arXiv:2503.17765
Geng J.-J., et al., 2025b, ApJ, 984, L65
Ghosh A., Razzaque S., Moskvitin A., Sotnikova Y., Dukiya N., Gupta R., 2025, GRB Coordinates Network, 39077, 1
Giannios D., Spitkovsky A., 2009, MNRAS, 400, 330
Granot J., Kumar P., 2006, Mon. Not. Roy. Astron. Soc., 366, L13
Granot J., Sari R., 2002, ApJ, 568, 820
HI4PI Collaboration et al., 2016, A&A, 594, A116
Huang Y. F., Dai Z. G., Lu T., 1999, MNRAS, 309, 513
Huang Y. F., Cheng K. S., Gao T. T., 2006, The Astrophysical Journal, 637, 873
Hussenot-Desenonges T., et al., 2024, Monthly Notices of the Royal Astronomical Society, 530, 1
Izzo L., Malesani D. B., Heintz K. E., Gompertz B., de Ugarte Postigo A., Hauptmann B. N., Kadela A. M., 2025, GRB Coordinates Network, 39073, 1
Jehin E., et al., 2018, The Messenger, 174, 2
Jockers K., et al., 2000, Kinematika i Fizika Nebesnykh Tel Supplement, 3, 13
Karpov S., 2021, STDPipe: Simple Transient Detection Pipeline (ascl:2112.006)
Karpov S., 2025, Acta Polytechnica, 65, 50–64
Kashikawa N., et al., 2004, PASJ, 56, 1011
Klotz A., Gendre B., Stratta G., Atteia J. L., Boër M., Malacrino F., Damerdji Y., Behrend R., 2006, A&A, 451, L39
Kouveliotou C., Meegan C. A., Fishman G. J., Bhat N. P., Briggs M. S., Koshut T. M., Paciesas W. S., Pendleton G. N., 1993, ApJ, 413, L101
Kumar P., Piran T., 2000, ApJ, 532, 286
Kumar P., Zhang B., 2015, Phys. Rep., 561, 1
Lang D., Hogg D. W., Mierle K., Blanton M., Roweis S., 2010, AJ, 139, 1782
Langarica R., et al., 2024, in Bryant J. J., Motohara K., Vernet J. R. D., eds, Society of Photo-Optical Instrumentation Engineers (SPIE) Conference Series Vol. 13096, Ground-based and Airborne Instrumentation for Astronomy X. p. 130963D, doi:10.1117/12.3020545
Laskar T., Berger E., Margutti R., Perley D., Zauderer B. A., Sari R., Fong W.-f., 2015a, ApJ, 814, 1
Laskar T., Berger E., Margutti R., Perley D., Zauderer B. A., Sari R., Fong W.-f., 2015b, ApJ, 814, 1
Laskar T., et al., 2018, ApJ, 859, 134
Lazzati D., Rossi E., Covino S., Ghisellini G., Malesani D., 2002, A&A, 396, L5
Li W., Filippenko A. V., Chornock R., Jha S., 2003, PASP, 115, 844
Li L., et al., 2012, ApJ, 758, 27
Li J.-D., Gao H., Ai S., Lei W.-H., 2024, The Astrophysical Journal, 978, 116
Liang E.-W., et al., 2013, ApJ, 774, 13
Luo J.-W., Wang F.-F., Zhu-Ge J.-M., Li Y., Zou Y.-C., Zhang B., 2023, The Astrophysical Journal, 959, 44
MacFadyen A. I., Woosley S. E., 1999, ApJ, 524, 262
MacFadyen A. I., Woosley S. E., Heger A., 2001, ApJ, 550, 410
Margutti R., et al., 2010, MNRAS, 402, 46
McCracken H. J., et al., 2003, A&A, 410, 17
Meszaros P., Rees M. J., 1993, ApJ, 405, 278
Metcalfe N., Shanks T., Campos A., McCracken H. J., Fong R., 2001, MNRAS, 323, 795
Moskvitin A., Spiridonova O., Sotnikova Y., Ghosh A., Razzaque S., 2025, GRB Coordinates Network, 39107, 1
Moss M. J., Mochkovitch R., Daigne F., Beniamini P., Guiriec S., 2023, Monthly Notices of the Royal Astronomical Society, 525, 5224
Nakar E., Granot J., 2007, MNRAS, 380, 1744
Narayan R., Paczynski B., Piran T., 1992, ApJ, 395, L83
Nardini M., et al., 2014, A&A, 562, A29
Nava L., Sironi L., Ghisellini G., Celotti A., Ghirlanda G., 2013, MNRAS, 433, 2107
Neights E., et al., 2025, arXiv e-prints, p. arXiv:2509.22792
Nousek J. A., et al., 2006a, ApJ, 642, 389
Nousek J. A., et al., 2006b, ApJ, 642, 389
Paczynski B., 1986, ApJ, 308, L43
Paczyński B., 1991, in Gamma-ray Bursts. AIP, pp 144–148, doi:10.1063/1.42815
Panaitescu A., Kumar P., 2000, ApJ, 543, 66
Panaitescu A., Meszaros P., Rees M. J., 1998, Astrophys. J., 503, 314
Pang P. T. H., et al., 2023, Nature Commun., 14, 8352
Pe'er A., 2012, ApJ, 752, L8
Pei Y. C., 1992, ApJ, 395, 130
Piran T., 1999a, Physics Reports, 314, 575
Piran T., 1999b, Phys. Rep., 314, 575
Piran T., 2004, Reviews of Modern Physics, 76, 1143
Ramirez-Ruiz E., Dray L. M., Madau P., Tout C. A., 2001, MNRAS, 327, 829
Rastinejad J. C., et al., 2022, Nature, 612, 223
Rees M. J., Meszaros P., 1998, Astrophys. J. Lett., 496, L1
Reichart D. E., 2006, Society for Astronomical Sciences Annual Symposium, 25, 39
Reichart D., et al., 2005, Nuovo Cimento C Geophysics Space Physics C, 28, 767
Rhoads J. E., 1999, ApJ, 525, 737
Roming P. W. A., Kennedy T. E., Mason K. O., et al., 2005, Space Science Reviews, 120, 95
Ryan G., van Eerten H., Piro L., Troja E., 2020, ApJ, 896, 166
Rybicki G. B., Lightman A. P., 1979, Radiative Processes in Astrophysics, 1st edn. Wiley-Interscience Publication, New York
Sari R., Mészáros P., 2000, ApJ, 535, L33
Sari R., Piran T., Narayan R., 1998, ApJ, 497, L17
Sari R., Piran T., Halpern J. P., 1999, ApJ, 519, L17
Scargle J. D., Norris J. P., Jackson B., Chiang J., 2013, ApJ, 764, 167
Schlafly E. F., Finkbeiner D. P., 2011a, The Astrophysical Journal, 737, 103
Schlafly E. F., Finkbeiner D. P., 2011b, ApJ, 737, 103
Schlekat D., Dutton D., Reichart D., Haislip J., Kouprianov V., 2025a, GRB Coordinates Network, 39091, 1
Schlekat D., Dutton D., Reichart D., Haislip J., Kouprianov V., Janzen D., Verveer A., Kennewell J., 2025b, GRB Coordinates Network, 39110, 1
Schmitt J., et al., 2024, A&A, 687, A198
Schneider B., et al., 2025a, GRB Coordinates Network, 39071, 1
Schneider B., et al., 2025b, GRB Coordinates Network, 39078, 1
Schneider B., et al., 2025c, GRB Coordinates Network, 39078, 1
Sebastian D., et al., 2021, A&A, 645, A100
Siegel M. H., Beardmore A. P., Swift/UVOT Team 2025, GRB Coordinates Network, 39085, 1
Srinivasaragavan G. P., et al., 2024, The Astrophysical Journal Letters, 960, L18
Steinhardt C. L., Mann W. J., Rusakov V., Jespersen C. K., 2023, ApJ, 945, 67
Sun T.-R., et al., 2024, ApJ, 976, L20
Uhm Z. L., Zhang B., 2014, Astrophys. J., 789, 39
Uhm Z. L., Zhang B., Hascoet R., Daigne F., Mochkovitch R., Park I. H., 2012, Astrophys. J., 761, 147
Wang X., Loeb A., 2000, ApJ, 535, 788
Wang H., Zhou H., Fan Y.-Z., Wei D.-M., 2025, ApJ, 990, 110
Watson A. M., et al., 2025a, GRB Coordinates Network, 39104, 1
Watson A. M., et al., 2025b, GRB Coordinates Network, 39136, 1
Waxman E., Piran T., 1994, ApJ, 433, L85
Willingale R., Starling R. L. C., Beardmore A. P., Tanvir N. R., O'Brien P. T., 2013, MNRAS, 431, 394
Woosley S. E., 1993, ApJ, 405, 273
Woosley S. E., Heger A., 2012, The Astrophysical Journal, 752, 32
Yu Y. W., Liu X. W., Dai Z. G., 2007, ApJ, 671, 637
Zhang B., Mészáros P., 2001, ApJ, 552, L35
Zhang B., Mészáros P., 2002, ApJ, 566, 712
Zhang B., Fan Y. Z., Dyks J., Kobayashi S., Mészáros P., Burrows D. N., Nousek J. A., Gehrels N., 2006, ApJ, 642, 354
de Ugarte Postigo, A. et al., 2018, A&A, 620, A190
van Eerten H., 2018, Int. J. Mod. Phys. D, 27, 1842002
van Eerten H. J., Meliani Z., Wijers R. A. M. J., Keppens R., 2009, MNRAS, 398, L63

[1] Université de la Côte d'Azur, Nice, France
[2] Center for Astrophysics and Space Science (CASS), New York University Abu Dhabi, Saadiyat Island, PO Box 129188, Abu Dhabi, UAE
[3] IJCLab, Univ Paris-Saclay, CNRS/IN2P3, Orsay, France
[4] E.Kharadze Georgian National Astrophysical Observatory, Mt. Kanobili, Abastumani, 0301 Adigeni, Georgia
[5] STAR Institute, Liege University, Allée du Six Août, 19C, B-4000 Liège, Belgium
[6] Department of Physics and Astronomy, University of North Carolina at Chapel Hill, Chapel Hill, NC 27599, USA
[7] Institute of Astronomy and NAO, Bulgarian Academy of Sciences, 72 Tsarigradsko Chaussee Blvd., 1784 Sofia, Bulgaria
[8] Department of Physics and Astronomy, University of North Carolina at Chapel Hill, Chapel Hill, NC 27599, USA
[9] School of Physics and Astronomy, University of Minnesota, Minneapolis, MN 55455, USA
[10] Université Paris Cité, CNRS, Astroparticule et Cosmologie, F-75013 Paris, France
[11] FZU - Institute of Physics of the Czech Academy of Sciences, Na Slovance 1999/2, CZ-182 21, Praha, Czech Republic
[12] National Research Institute of Astronomy and Geophysics (NRIAG), 1 El-marsad St., 11421 Helwan, Cairo, Egypt
[13] Université de Strasbourg, CNRS, IPHC UMR 7178, F-67000 Strasbourg, France
[14] Université Paris-Saclay, Université Paris Cité, CEA, CNRS, AIM, 91191, Gif-sur-Yvette, France
[15] Aix Marseille Univ., CNRS, CNES, LAM, Marseille, France
[16] GEPI, Observatoire de Paris, Université PSL, CNRS, 5 place Jules Janssen, 92190 Meudon, France
[17] Physics Department, Eastern Illinois University, Charleston, IL, 61920, USA
[18] Instituto de Astronomía, Universidad Nacional Autónoma de México, Apartado Postal 70-264, 04510 México, CDMX, México
[19] School of Earth and Space Exploration, Arizona State University, PO Box 871404, Tempe AZ 85287, USA
[20] Aix-Marseille Univ., CNRS/IN2P3, Ctr. de Physique des Particules de Marseille, IPhU (France)
[21] Università degli Studi di Roma Tor Vergata, Roma, Italy
[22] Facultad de Ciencias, Universidad Nacional Autónoma de México, Apartado Postal 70-264, 04510 México, CDMX, México
[23] Purple Mountain Observatory, Chinese Academy of Sciences, Nanjing 210023, China
[24] School of Astronomy and Space Sciences, University of Science and Technology of China, Hefei 230026, China
[25] Nanjing Institute of Astronomical Optics & Technology, National Astronomical Observatories, Chinese Academy of Sciences, Nanjing 210042, China
[26] Department of Astronomy, University of California, Berkeley, CA 94720-3411, USA
[27] SOAR Telescope/NSF's NOIRLab, Avda Juan Cisternas 1500, 1700000, La Serena, Chile
[28] Laboratório Nacional de Astrofísica - LNA, Rua Estados Unidos, 154 Itajubá - MG CEP 37504-364, Brazil
[29] Universidade do Estado do Amazonas - UEA, Parintins, Amazonas, Brazil
[30] ASU - Astronomical Institute of the Czech Academy of Sciences, Fričova 298, 251 65 Ondřejov, Czech Republic
[31] Montarrenti Observatory, S.S. 73 Ponente, I-53018, Sovicille, Siena, Italy
[32] Instituto de Astronomía, Universidad Nacional Autónoma de México, km 107 Carretera Tijuana-Ensenada, 22860 Ensenada, Baja California, México
[33] AITP, 3 rue sainte odile, 67560 Rosheim, France
[34] European Southern Observatory, Alonso de Córdova 3107, Vitacura, Santiago, Chile
[35] Institute of Physics, Laboratory of Astrophysics, Ecole Polytechnique Fédérale de Lausanne (EPFL), Observatoire de Sauverny, 1290 Versoix, Switzerland
[36] IRAP, Université de Toulouse, CNRS, CNES, UPS, France
[37] Colfax 54730. United States, WI. NA, USA
[38] Al-Khatim Observatory, AKO, operated by the International Astronomical Center in Abu Dhabi, UAE
[39] Department of Physics, Lancaster University, Lancaster, LA1 4YB, UK
[40] Department of Earth, Atmospheric and Planetary Science, Massachusetts Institute of Technology, 77 Massachusetts Avenue, Cambridge, MA 02139, USA
[41] Astrobiology Research Unit, Université de Liège, Allée du 6 Août 19C, B-4000 Liège, Belgium
[42] Instituto de Astrofísica de Canarias (IAC), Calle Vía Láctea s/n, 38200, La Laguna, Tenerife, Spain
[43] Université Côte d'Azur, Observatoire de la Côte d'Azur, CNRS UMR 7293 Laboratoire Lagrange, F 06108 Nice, France
[44] LTE , Observatoire de Paris, PSL Research University, Sorbonne Université, CNRS, 77 av. Denfert-Rochereau, Paris, 75014, France
[45] Instituto de Ciencias Nucleares, Universidad Nacional Autónoma de México, Apartado Postal 70-264, 04510 México, CDMX, Mexico
[46] Instituto de Radioastronomía y Astrofísica, Universidad Nacional Autónoma de México, Antigua Carretera a Pátzcuaro # 8701, Ex-Hda. San José de la, Huerta, Morelia, Michoacán, México C.P. 58089, Mexico
[47] Institute of Physics and Astronomy, Theoretical Astrophysics, University Potsdam, Haus 28, Karl-Liebknecht-Str. 24/25, 14476
[48] Nikhef, Science Park 105, 1098 XG Amsterdam, The Netherlands
[49] Institute for Gravitational and Subatomic Physics (GRASP), Utrecht University, Princetonplein 1, 3584 CC Utrecht, The Netherlands
[50] Max Planck Institute for Gravitational Physics (Albert Einstein Institute), Am Mühlenberg 1, Potsdam 14476, Germany
[51] Department of Physics Astronomy, University of Utah, Salt Lake City, UT 84112, USA
[52] Department of Astrophysics/IMAPP, Radboud University, PO Box 9010, 6500 GL Nijmegen, The Netherlands
[53] Cahill Center for Astrophysics, California Institute of Technology, MC 249-17, 1216 E California Boulevard, Pasadena, CA, 91125, USA
[54] Xinjiang Astronomical Observatory, Chinese Academy of Sciences, Urumqi, Xinjiang, 830011, China
[55] School of Astronomy and Space Science, University of Chinese Academy of Sciences, Beijing 100049, China
[56] Physics Department, Tsinghua University, Beijing, 100084, China
[57] Laboratoire de Physique de l'E´cole Normale Sup´erieure, ENS, Universit´e PSL, CNRS, Sorbonne Universit´e, Universit´e de Paris, 75005 Paris, France
[58] Department of Physical Sciences, Embry-Riddle Aeronautical University, 1 Aerospace Boulevard, Daytona Beach, Fl 32114, USA
[59] NEPA, Universidade do Estado do Amazonas (UEA), 69.152-510, Parintins, Brasil
[60] American University of Sharjah, Physics Department, PO Box 26666
[61] Astronomy and Space Physics Department, Taras Shevchenko National University of Kyiv, 4 Glushkova ave., Kyiv, 03022 Ukraine 35 National Center "Junior Academy of Sciences of Ukraine", 38-44 Dehtiarivska St., Kyiv, 04119 Ukraine
[62] National Astronomical Research Institute of Thailand (NARIT), Chiang Mai 50180, Thailand.
[63] Department of Physics, University Rio Grande do Norte, Rio Grande do Norte, Brazil
[64] New York University Abu Dhabi, PO Box 129188, Saadiyat Island, Abu Dhabi, UAE
[65] Yunnan Observatories, Chinese Academy of Sciences, 650011 Kunming, Yunnan Province, China
[66] School of Physics and Astronomy, Beijing Normal University, Beijing, 100875, China

[67] University of Tampa, Department of Physics and Astronomy, 401 W. Kennedy Blvd, Tampa, FL 33606, USA
[68] Department of Astronomy, University of Maryland, College Park, 7901 Regents Drive College Park, MD 20742, USA
[69] Physics Department, Nazarbayev University, 53 Kabanbay Batyr Ave., Astana 010000, Kazakhstan
[70] Energetic Cosmos Laboratory, Nazarbayev University, 53 Kabanbay Batyr Ave., Astana 010000, Kazakhstan

Appendix A: Contribution

D. Akl and S. Antier are the main contributors to the work, including the analysis and writing across all sections, coordination, and organization of contributors related to observational and high-energy results. M. Pillas was the chair of the GRB program and manages the article on behalf of GRANDMA.

Z. Wang, S. Antier, A. Klotz are the main authors of Sec. 2.1. They received help from A. Lien.

D. Akl and M. Molham are the main contributors and authors of Sec. 2.2. D. Akl and M. Molham are the authors of Sec. 2.3 related to Space observations with the help of S. Oates and A. de Ugarte Postigo, and D. Akl is the main author related to Ground observations, with the coordination and contribution of S. Antier and S. Karpov.

N. Rakotondrainibe is the main contributor of Sec. 3.1. R. L. Becerra is the main contributor of Sec. 3.2.

J. Mao, R. Strausbaugh, E. Abdikamalov, and D. Berdikhan are the main authors of Sec. 4.1. P. Pang and H. Koehn are members of the paper writing team and wrote Sec. 4.2. J.J Geng is the main contributor of Sec. 4.3. R. Gill and T. Laskar contributed to reviewing Sec. 4 as well as guiding the modeling of the rebrightening episodes.

C. Adami, Q. André S. Antier, V. Aivazyan, K. Barkaoui, P. Bendjoya, E. Bernaud, S. Brunier, A.Y. Burdanov, J. Chen, F. Colas, D. Darson, A. Durroux, D. Dutton, F. Dux, A. Esamdin, A.V. Filippenko, M. Freeberg, J.J. Geng, M. Gillon, R. Hellot, Y. Hendy, Y.L. Hua, R. Inasaridze, A. Iskandar, M. Jelínek, S. Karpov, A. Klotz, N. Kochiashvili, S. Leonini, X.Y. Li, C. Limonta, J. Liu, M. Mašek, B.M. Mihov, M. Molham, M. Odeh, D. Reichart, J.-P. Rivet, F. Romanov, D. Schlekat, L. Slavcheva-Mihova, T.R. Sun, A. Saccardi, A. Takey, D. Turpin, L.T. Wang, X.F. Wang, Y.S. Yan, J. de Wit, S. Zúñiga-Fernández, W. Zheng contributed to this work via observations and measurements taken by various GRANDMA/KNC observatories and their partners as KAIT and SkyNet.

N. Globus, N. Guessoum, E. Abdikamalov and N. Kochiashvili contributed to the review and editing of the full article to improve the quality of the article.

Appendix B: Acknowledgements (extended)

D. Akl is supported by Tamkeen under the NYU Abu Dhabi Research Institute grant CASS.

P.T.H.P. is supported by the research program of the Netherlands Organization for Scientific Research (NWO) under grant number VI.Veni.232.021.

We thank the staff of the Observatorio Astronómico Nacional on Sierra San Pedro Mártir.

TAROT has been built with the support of the Institut National des Sciences de l'Univers, CNRS, France. TAROT is funded by the CNES and thanks to the help of the technical staff of the Observatoire de Haute-Provence, OSU-Pytheas.

EA's and DB's work was funded by the Science Committee of the Ministry of Science and Higher Education of the Republic of Kazakhstan (Grant No. AP26103591). EA acknowledges support by the Nazarbayev University Faculty Development Competitive Research Grant Program (no. 040225FD4713).

We would like to thank the Pierre Auger Collaboration for the use of its facilities.

This work made use of data supplied by the UK *Swift* Science Data Centre at the University of Leicester.

CAV acknowledges support from a SECIHTI fellowship.

DGS acknowledges support from a NASA North Carolina Space Grant Undergraduate Research Scholarship.

RLB acknowledges support from the European Research Council through the Consolidator grant BHianca (grant agreement ID 101002761).

AbAO team acknowledges Shota Rustaveli National Science Foundation of Georgia (SRNSFG). This work was supported by SRNSFG grant FR-24-7713.

BMM and LS-M research was carried out with the help of infrastructure renovated under the National Roadmap for Research Infrastructure (2020-2027), financially coordinated by the Ministry of Education and Science of Republic of Bulgaria (agreement D01-326/04.12.2023).

Based in part on observations made at Observatoire de Haute Provence (CNRS), France, with MISTRAL. This research has made use of the MISTRAL database, operated at CeSAM (LAM), Marseille, France.

The Virgin Islands Robotic Telescope (VIRT) is located at the University of the Virgin Islands' (UVI's) Etelman Observatory on St. Thomas, U.S. Virgin Islands. UVI operates VIRT and uses it for robotic optical observations in support of time-domain and transient astronomy, including GRANDMA follow-up campaigns. The observatory acknowledges support in part from NASA EPSCoR 80NNSC22M0063, NSF AST 2319415, and NASA EPSCoR 80NSSC24M0112.

The KAO-NRIAG team acknowledges financial support from the Egyptian Science, Technology & Innovation Funding Authority (STDF) under grant number 45779. M. Molham acknowledges the support provided by the Women for Africa Foundation, whose contribution enabled the tools and methodologies applied in this work. KAO thanks M. Abdelkareem for conducting observations.

The AST3-3 and YAHPT team would like to express their sincere thanks to the staff of the Yaoan observation station.

M.G. and E.J. are FNRS-F.R.S. Research Directors. J.d.W. and MIT gratefully acknowledge financial support from the Heising-Simons Foundation, Dr. and Mrs. Colin Masson, and Dr. Peter A. Gilman for Artemis, the first telescope of the SPECULOOS network situated in Tenerife, Spain. The ULiege's contribution to SPECULOOS has received funding from the European Research Council under the European Union's Seventh Framework Programme (FP/2007-2013) (grant Agreement n° 336480/SPECULOOS), from the Balzan Prize and Francqui Foundations, from the Belgian Scientific Research Foundation (F.R.S.-FNRS; grant n° T.0109.20), from the University of Liege, and from the ARC grant for Concerted Research Actions financed by the Wallonia-Brussels Federation.

J.G is supported by the National Natural Science Foundation of China (grant Nos. 12273113, 12393812, 12393813, and 12321003), the Strategic Priority Research Program of the Chinese Academy of Sciences (grant No. XDB0550400), and the Youth Innovation Promotion Association (2023331).

J.M is financially supported by the National Key R&D Program of China (2023YFE0101200), Natural Science Foundation of China 12393813, and the Yunnan Revitalization Talent Support Program (YunLing Scholar Project).

S.K. acknowledges financial support from the European Union and the Czech Ministry of Education, Youth and Sports (Project No. CZ.02.01.01/00/22_008/0004632 – FORTE).

FRAM-Auger telescope operation is supported by the Czech Ministry of Education, Youth and Sports (projects MEYS LM2018105, LM2023047, and EU/MEYS CZ.02.01.01/00/22_008/0004632).

Members of TNOT acknowledge financial support from the Natural Science Foundation of Xinjiang Uygur Autonomous Re-

gion under No. 2024D01D32; Tianshan Talent Training Program grant 2023TSYCLJ0053. X. Wang is supported by NSFC (12288102, 12033003) and Tecent Xplorer Prize.

NG and LGG gratefully acknowledge the support of the Simons Foundation (MP-SCMPS-00001470, N.G., L.G.G).

Appendix C: X-ray Data Reduction: Additional Details

We rebinned the XRT light curve into non-contiguous segments. Each of these segments was treated as a distinct temporal window, within which we calculated the mean flux and its standard deviation. This approach allows us to combine temporally proximate measurements, hence increasing the signal-to-noise ratio of temporally close data points and retaining the overall time evolution of the light curve. For each bin, we calculated the average time in the bin, average flux density, and the error on the flux density, which was calculated as the larger of the standard deviation of the flux values or the average propagated error.

To convert the flux density from 10 keV to 2 keV, and derive the AB magnitudes, we used the standard energy scaling relation for flux densities in frequency space:

$$F_\nu(E_2) = F_\nu(E_1)\left(\frac{E_2}{E_1}\right)^{\Gamma-1},$$

where E_1 = 10 keV, E_2 = 2 keV, and $\Gamma - 1 = 0.94$ for the photon index $\Gamma = 1.94$, obtained from the online Swift Time-Averaged Spectrum footnote`https://www.swift.ac.uk/xrt_spectra/01285812/`.

This conversion is motivated by the fact that *Swift*-XRT's effective area, and hence its sensitivity, declines significantly at higher energies, making 10 keV flux measurements noisier and less reliable. We selected 2 keV as a reference energy for spectral scaling and magnitude conversion, as it lies near the logarithmic midpoint of the *Swift*-XRT energy band (0.3–10 keV).

The output flux values were subsequently converted to AB magnitudes using the standard relation:

$$m_{AB} = -2.5\log_{10}\left(\frac{F_\nu}{3631\ \mathrm{Jy}}\right)$$

where F_ν is the flux at 2keV in Jy and 3631 Jy corresponds to the flux density of an object with an AB magnitude of 0.

The data reduction and spectral analysis were conducted using `HEASoft v6.34` using the *XRT tool xrtpipeline (v0.13.7)* on the three XRT spectra on 2025-01-29, with the latest updated calibration data files (`CALDB`, released on 2024 February 28). Spectral modeling and parameter estimation were performed using `XSPEC v12.14.1`, employing c-statistics as the fitting method (`Fit.statMethod = "cstat"`), which is particularly suited for low-count Poisson-distributed X-ray data as it provides a more reliable parameter estimation compared to the traditional χ^2 fitting, which assumes Gaussian errors.

XRT spectra [0.3-10 keV] were extracted from circular regions (`25-arcsec`) around the source center and background regions (`50 arcsec`) away from the source, grouped such that the source spectrum contained at least 1 count per bin. The spectra were fitted with an absorbed power-law model, with the galactic column density ($N_H = 2.4 \times 10^{20}$ cm^{-2}) (Dickey & Lockman 1990) fixed, using the TBabs model of Wilms, Allen & McCray(2001), leaving only the photon index and the normalization as free parameters. Spectra were fit in the 0.3 to 10.0 keV energy range. Using the photon index from the fitting and the normalization, the spectral model used for fitting is defined as `tbabs*powerlaw`, where `tbabs` represents the Tübingen-Boulder absorption model, accounting for interstellar photoelectric absorption characterized by the neutral hydrogen column density (N_H), while `powerlaw` describes the X-ray emission as a simple power-law function.

The best-fit photon indices for the three source spectra within the first day were $\Gamma = 1.99 \pm 0.23$, $\Gamma = 2.15 \pm 0.15$, and $\Gamma = 1.87 \pm 0.18$, respectively. The corresponding flux at `2 keV` was 2.75×10^{-11} erg cm^{-2} s^{-1}, 8.51×10^{-11} erg cm^{-2} s^{-1}, and 6.53×10^{-11} erg cm^{-2} s^{-1}, obtained from the fitted spectral parameters.

Appendix D: Optical Observations

Appendix D.1: Optical Observations

In this section, we detail observations for GRB 250129A by GRANDMA and its associated partners. Early observations of the optical afterglow of GRB 250129A started on MJD 60704.20 using the TAROT-TCA and TAROT-TCH [7] telescopes, two robotic 25 cm aperture telescopes located at the Calern Observatory (Observatoire de la Côte d'Azur) and La Silla Observatory, respectively, detected the afterglow at $T - T0 = 106s$.

The full observational campaign lasted 24.23 days. We use for this work the data obtained in g', r', i', z', B, V, R, I bands for extracting the physical properties of the event. We provide in Table D.1 a list of all the telescopes involved in the observational campaign, including the start and end times (relative to $T0$) of the first and last observations made by each telescope. We also provide the filters/bands used during the entire campaign. Below, we provide details on all the telescopes that are involved in this study.

The telescopes that contributed to this campaign are as follows: AbAO T-70 Telescope at Abastumani Observatory in Georgia, the ground-based ARTEMIS telescope of the SPECULOOS Northern Observatory (SNO) in Spain, Colibri at San Pedro Martir, C2PU at Calern observatory, Euler telescope at La Silla, FRAM-Auger telescope at Pierre Auger observatory in Argentina, KAIT telescope at Lick Observatory in California, KAO at Kottamia Observatory in Egypt, T193/MISTRAL at Haute-Provence Observatory in France, NAO-2m at Rozhen National Astronomical Observatory in Bulgaria, OPD-0.6m at the Pico dos Dias's Observatory in Brazil, Pic du Midi 1-m Telescope at Pic du Midi observatory in France, Skynet Network, TAROT-TCA located at the Calern observatory in France, TAROT-TCH located at La Silla, TNOT telescope located at the Nanshan Station of Xinjiang Astronomy Observatory in China, YAHPT/AST3-3. Our preliminary results were reported publicly through the General Coordinates Network (GCN)[8] by (Schlekat et al. 2025a), (Antier et al. 2025), (Watson et al. 2025a), (Akl et al. 2025a), (Schlekat et al. 2025b), and (Akl et al. 2025b).

KNC– In addition to the professional network, GRANDMA activated its Kilonova-Catcher (KNC) citizen science program for further observations with amateurs' telescopes. Seven amateur telescopes observed GRB 250129A, including nicknames Monaterrenti, CAT, MLC, AITP, T11, T30, CH!CMOS, and CDK. Overall, the KNC telescopes started observing from $T - T0 = 0.857$ days up to $T - T0 = 3.108$ days. Photometry

[7] `http://tarot.obs-hp.fr/`
[8] `https://gcn.nasa.gov/`

of KNC images followed the same methodology detailed in Section 2.3.

Abastumani T-70– AbAO T-70 Telescope at Abastumani Observatory in Georgia, with the main mirror diameter of 100 cm located on the Mt. Kanobili (altitude 1610 m above sea level; 41° 45′ 17″ N, 42° 49′ 20″ E) and equipped with a pl4240-ccd-camera-back-illum-63-5mm-shutter-grade-1 with BVR_cI_c filters provides an FOV of 30′, with a readout of 10 s. The limiting magnitude in the R_c filter with an exposure time of 1 min is 18.2 mag (AB system, 3σ).

Artemis SPECULOOS-North/Artemis (Burdanov et al. 2022) is a 1.0-m Ritchey-Chrétien telescope located at the Teide Observatory (Tenerife, Spain). It is equipped with a thermoelectrically cooled 2K×2K Andor iKon-L BEX2-DD CCD camera with a pixel scale of 0.35″/pixel and a total FOV of $12' \times 12'$. SPECULOOS-North is a twin of the SPECULOOS-South (Jehin et al. 2018; Delrez et al. 2018; Sebastian et al. 2021) and SAINT-EX (Demory et al. 2020) telescopes. Observations were performed with the SDSS g', r', z' filters.

C2PU– C2PU is a two 1.04-meter telescopes facility of Observatoire de la Côte d'Azur located at the Calern observing station in Southern France (longitude : 06° 55′ 22.7″ E, latitude : 43° 45′ 13.2″ N, elevation : 1274 m above MSL, IAU observatory code : $R87$)[9]. For this photometric follow-up, the West "Omicron" telescope of C2PU has been used in its $F/3.17$ optical configuration (parabolic prime focus with a three-lens Wynne corrector). The camera used was a QHY600 from QHYCCD (CMOS sensor Sony IMX455 with 9600×6422 pixels of 3.76×3.76 μm) in binning 2×2. The resulting plate scale and field-of-view were 0.47″/pixel, and $37.6' \times 25.2'$.

COLIBRÍ– COLIBRÍ[10] is a Franco-Mexican fast, robotic 1.3 m telescope located at the Observatorio Astronómico Nacional (OAN) in the Sierra de San Pedro Mártir, Baja California (Basa et al. 2022). COLIBRI used the blue channel of the DDRAGO science imager(Langarica et al. 2024) and the OGSE camera.

OGSE is an ON Semi KAF-16803 front-illuminated CCD in an FLI ML 16803 package. The CCD is 4k × 4k with 9 pixels. The pixel scale is 0.20 arcsec/pixel, and the field is 13.6 arcmin square. OGSE is equipped with a fixed Baader red filter that transmits from 590 to 690 nm. This filter is narrower and redder than the standard SDSS/Pan-STARRS r filter; the color term in the transformation is $-0.10(g - r)$.

DDRAGO is a two-channel image with the blue channel working in g, r, i and the red in z, y (Langarica et al. 2024). During COLIBRI observations, the red channel was not available. The blue channel uses a backside-illuminated, deep-depleted e2v 231-84 CCD in a Spectral Instruments 1110S package. The CCD is 4k × 4k with 15 pixels. The pixel scale is 0.38 arcsec/pixel, and the field is 25.9 arcmin square. All of our observations were performed with the r filter, which closely approximates SDSS/Pan-STARRS r; the color term in the transformation is smaller than $0.01(g - r)$.

Euler– The 1.2-metre Euler Telescope is located at La Silla, built and operated by the Geneva Observatory, Université de Genève, Switzerland. The Euler Telescope is equipped with three complementary instruments: the CORALIE spectrograph, the EulerCam (ECAM), and PISCO, a smaller telescope mounted piggyback on the Euler Telescope.

FRAM-Auger– FRAM-Auger is a fully robotic 30 cm f/6.8 telescope located at the Pierre Auger Observatory, Malargue, Argentina. The telescope is equipped with Moravian Instruments G4-16000 CCD, and B, V, R, and I filters, and has a field of view of 60′x60′, with a pixel scale of 0.92″/ arcseconds per pixel.

KAIT– The 0.76 m Katzman Automatic Imaging Telescope (KAIT), located at the Lick Observatory, California (as part of the Lick Observatory Supernova Search (LOSS; Filippenko et al. 2001)), observed the field of the GRB 250129A from $T - T0 = 0.196$ days to $T - T0 = 1.393$ days. Observations were performed in the $Clear$-band (close to the R band; see Li et al. 2003) with a set of 60 s-exposure images.

KAO– The KAO data presented in this study were acquired using the 1.88-m telescope at the Kottamia Astronomical Observatory (KAO), operated by the National Research Institute of Astronomy and Geophysics (NRIAG), Egypt (Azzam et al. 2010). These observations utilized the Kottamia Faint Imaging Spectro-Polarimeter (KFISP), an instrument capable of imaging, spectroscopy, and polarimetry (Azzam et al. 2022). KFISP is mounted at the Cassegrain focus of the telescope and provides a field of view of approximately 8.2 × 8.2 arcminutes. It is equipped with a 2048 × 2048 pixel liquid nitrogen-cooled CCD camera integrated within the KFISP optics, yielding a pixel scale of 0.24 arcseconds per pixel.

NAO-2m– NAO-2m denotes the 2-m Ritchey-Chrétien telescope of the Rozhen National Astronomical Observatory, Bulgaria. For the present observations, the telescope was equipped with the multi-mode, two-channel focal reducer FoReRo-2 (Jockers et al. 2000), 2k × 2k Andor iKon-L CCD cameras, and a Sloan set of filters. The gain is $1.0\,e^-\,ADU^{-1}$ for the blue channel CCD and $1.1\,e^-\,ADU^{-1}$ for the red channel one. For both channels, the pixel size is 0.″497 on the sky and the field-of-view is $17' \times 17'$. Ten or more frames were acquired of the GRB 250129A field in each of the $g'r'i'$ bands with exposure times of 300 or 600 s.

OHP/MISTRAL– MISTRAL (Multi-purpose InSTRument for Astronomy at Low resolution, Schmitt et al. (2024)) is a Faint Object Spectroscopic Camera mounted at the folded Cassegrain focus of the 1.93 m telescope of the Haute-Provence Observatory (OHP). Present observations were made in the blue mode (400–800 nm) during four observing slots. We used r' and i'-band filters[11]. The CCD is an ANDOR deep-depletion 2K×2K CCD camera (iKon-L DZ936N BEX2DD CCD-22031) with 13.5 pixels. The cooling is made by a five-layer Peltier device. The operating temperature is −90°C to −95°C. The dark current is lower than 3 electrons/hour/pixel. More details can be found on the instrument website[12].

[9] https://www.oca.eu/fr/c2pu-accueil
[10] https://www.colibri-obs.org/
[11] https://ohp.osupytheas.fr/wp-content/uploads/2025/04/filter_characteristics.html
[12] https://ohp.osupytheas.fr/mistral-spectro-imager/

Pic Du Midi– Pic du Midi 1-m Telescope at Pic du Midi observatory in France. The telescope is equipped with two cameras. The first one is an ANDOR 2K×2K CCD camera (iKon-L DZ936) with a spatial sampling of 0.5 arcsec/pixel. The second camera is a LYTID Siris [13] InGaAs sensor FPA 640x512 pixels, with a spatial sampling of read-out noise of 5 electrons, operated at 77 K.

Skynet– The Skynet Robotic Telescope Network[14] (Skynet) is a fully automated global network of optical and radio telescopes used for both education and research. Founded and operated out of the University of North Carolina at Chapel Hill, Skynet is comprised of the Panchromatic Robotic Optical Monitoring and Polarimetry Telescopes (PROMPT; Reichart et al. 2005), which were originally dedicated to rapid-response observations of GRBs (Reichart 2006), as well as various other optical telescopes from participating institutions across the globe.

Approximately one minute after the *Swift-BAT* trigger time (2025-01-29 4:45:09), Skynet's `Campaign Manager` software (Dutton et al. 2022) automatically scheduled observations of the field of GRB 250129A on all available Skynet telescopes. The field of the GRB was subsequently observed using the 40 cm PROMPT-2, PROMPT-5 and PROMPT-6 telescopes at the Cerro Tololo Inter-American Observatory, the 40 cm PROMPT-MO-1 telescope at Meckering Observatory, the 40 cm MLC-RCOS16 telescope at the Montana Learning Center, the 50 cm OAUJ-CDK500 telescope at the Astronomical Observatory of the Jagiellonian University, and 40 cm the APUS-CDK24 telescope (Albin 2018) at the American Public University System Observatory.

TNOT– The Tsinghua-Nanshan Optical Telescope, an 80-cm aperture reflector telescope located at Nanshan Station of Xinjiang Astronomy Observatories (XAO), Chinese Academy of Sciences (CAS). The field of view was designed to 26.5" × 26.5", and the Bessel BV system and Sloan ugri system were chosen as the main filter set. The imaging system utilizes an Andor iKon-L DZ936 CCD camera with a 2048 × 2048 pixel array, and the pixel scale is 0.78 arc seconds.

YAHPT/AST3-3– The YaoAn High Precision Telescope (YAHPT) is an 80-cm diameter automatic telescope manufactured by ASA and deployed at the YaoAn Astronomical Station in Yunnan Province. Equipped with a PIXIS 2024B camera, it provides a field of view of $11'' \times 11''$ and is dedicated to high-precision astrometric measurements of natural satellites and asteroids. The third Antarctic Survey Telescope (AST3-3, 68 cm Schimdt) was also temporarily deployed at the YaoAn station for commissioning before its final deployment to Dome A, Antarctica. AST3-3 is now equipped with a QHY411 camera featuring a Sony IMX-411 sensor, offering a field of view of 1.65° × 1.23° with a 14 K × 10 K pixel array. The basic data processing for both YAHPT and AST3-3 follows the standard CCDPROC procedures, with astrometric calibration based on the Gaia DR3 catalog.

Instrument	$T-T0_{start}$	$T-T0_{end}$	Bands
TAROT/TCH	< 0.001	0.140	R
FRAM-Auger	0.008	0.090	R
Skynet-PROMPT-5	0.019	3.165	B, V, R
Skynet-PROMPT-6	0.019	3.166	B, V, R, I
OHP/MISTRAL	0.038	7.992	r', i'
KAIT	0.196	1.393	R
Skynet-MLC	0.201	0.233	R
TNOT	0.646	4.816	g', r'
Skynet-OUAJ	0.806	1.835	R
KAO	0.847	0.874	g', r', i', z'
KNC-Montarrenti	0.857	0.8570	R, I
KNC-AITP	1.034	3.092	V, g', r', i'
Skynet-APUS	1.061	1.128	R
COLIBRI	1.141	24.234	r'
KNC-T11	1.317	1.329	R, V
KNC-T30	1.529	-	R
AbAO-T70	1.730	2.767	R
KNC-CH!CMOS	2.126	3.108	g', r'
Skynet-PROMPT-MO	2.500	2.507	R
Skynet-PROMPT-2	3.011	3.168	I
KNC-CDK	3.018	-	V
Euler	3.115	10.158	R, i'
AST3-3	3.648	4.573	g'
YAHPT	3.571	4.595	I
NAO-2m	4.884	4.951	g', r', i'
T-CAT	5.836	-	V, g', r'
C2PU	5.884	5.970	g', r', i', z'
Artemis	6.009	7.039	g', r', z'
PicDuMidi-T1M	6.994	7.885	g', r', J
OPD-T60	8.100	22.049	R, I

Table D.1. All observational instruments whose data have been analyzed and incorporated into the results presented in this study. The $T - T_0$ provided is in days.

[13] `https://lytid.com/wp-content/uploads/2024/06/SIRIS-brochure-June-2024.pdf`
[14] `https://skynet.unc.edu/`

Table D.2. X-ray data used in this work. "Delay" is the time interval between the start of the observation (T_{start}) and the Swift GRB trigger time (2025-01-29T04:45:09). We display both the unabsorbed flux densities and the corresponding computed AB magnitudes.

$T_{\rm start}$		Delay		Band	Flux			Instrument
UT	MJD	(day)	(s)	Central frequency	AB Magnitude	Flux density (μJy)	Error (μJy)	
X-ray bands								
2025-01-29T05:04:53	60704.212	0.014	1185	2keV	24.27 ± 0.24	0.711	0.16	Swift XRT
2025-01-29T05:06:32	60704.213	0.015	1284	2keV	24.14 ± 0.24	0.804	0.18	Swift XRT
2025-01-29T05:08:05	60704.214	0.016	1376	2keV	23.76 ± 0.25	1.140	0.26	Swift XRT
2025-01-29T05:10:00	60704.215	0.017	1491	2keV	23.88 ± 0.24	1.019	0.23	Swift XRT
2025-01-29T05:11:54	60704.217	0.019	1605	2keV	24.02 ± 0.25	0.896	0.20	Swift XRT
2025-01-29T05:14:10	60704.218	0.020	1742	2keV	24.23 ± 0.25	0.741	0.17	Swift XRT
2025-01-29T05:16:28	60704.220	0.022	1879	2keV	24.14 ± 0.21	0.802	0.16	Swift XRT
2025-01-29T06:16:42	60704.262	0.064	5493	2keV	24.65 ± 0.23	0.503	0.10	Swift XRT
2025-01-29T07:53:25	60704.329	0.131	11297	2keV	24.99 ± 0.23	0.367	0.08	Swift XRT
2025-01-29T09:23:47	60704.392	0.194	16719	2keV	24.64 ± 0.28	0.505	0.13	Swift XRT
2025-01-29T11:04:33	60704.461	0.263	22765	2keV	24.39 ± 0.23	0.637	0.13	Swift XRT
2025-01-29T12:41:03	60704.529	0.330	28554	2keV	24.80 ± 0.25	0.436	0.10	Swift XRT
2025-01-29T14:09:34	60704.590	0.392	33865	2keV	25.24 ± 0.31	0.292	0.08	Swift XRT
2025-01-30T05:41:43	60705.237	1.039	89795	2keV	27.52 ± 0.20	0.036	0.01	Swift XRT
2025-02-01T02:16:30	60707.095	2.897	250281	2keV	28.92 ± 0.23	0.010	0.00	Swift XRT
2025-02-05T20:07:18	60711.838	7.640	660130	2keV	30.77 ± 0.33	0.002	0.00	Swift XRT
2025-02-09T12:25:46	60715.518	11.320	978038	2keV	31.41 ± 0.51	0.001	0.00	Swift XRT

Table D.3. UVOIR observations of GRB 250129A. In column (2), $T_{(s)}$ is the time delay between the start of the observation and the *Swift* GRB trigger time (2025-01-29T04:45:09), all in days. Column (4) gives apparent magnitudes or 5-σ upper-limits in the AB system, without any correction. In Column (7), a cross means we did use this data point for the Bayesian analysis.

$T_{\rm start}$		$T - T_{GRB}$		Filter	Magnitude	Corrected Magnitude	Telescope	Analysis
UT	MJD	Day	Minute					
(1)		(2)		(3)	(4)	(5)	(6)	(7)
uv band								
2025-01-29T04:47:42	60704.200	0.002	2.557	*v*	17.58±0.45	17.48±0.45	*UVOT*	x
2025-01-29T05:06:08	60704.213	0.015	20.987	*white*	18.19±0.06	18.04±0.06	*UVOT*	
2025-01-29T05:07:41	60704.214	0.016	22.535	*v*	16.73±0.21	16.64±0.21	*UVOT*	x
2025-01-29T05:09:21	60704.215	0.017	24.216	*b*	17.10±0.17	16.97±0.17	*UVOT*	x
2025-01-29T05:09:46	60704.215	0.017	24.625	*white*	18.14±0.10	17.99±0.10	*UVOT*	
2025-01-29T05:09:58	60704.215	0.017	24.828	*uvw1*	19.55±0.35	19.34±0.35	*UVOT*	
2025-01-29T05:10:23	60704.216	0.018	25.242	*u*	18.03±0.14	17.87±0.14	*UVOT*	x
2025-01-29T05:10:35	60704.216	0.018	25.449	*v*	16.97±0.27	16.88±0.27	*UVOT*	x
2025-01-29T05:12:15	60704.217	0.019	27.112	*b*	16.86±0.16	16.73±0.16	*UVOT*	x
2025-01-29T05:12:39	60704.217	0.019	27.516	*white*	18.17±0.12	18.01±0.12	*UVOT*	
2025-01-29T05:15:07	60704.219	0.021	29.983	*b*	17.25±0.23	17.13±0.23	*UVOT*	x
2025-01-29T05:15:33	60704.219	0.021	30.407	*white*	18.10±0.12	17.95±0.12	*UVOT*	
2025-01-29T05:15:45	60704.219	0.021	30.609	*uvw1*	19.36±0.36	19.15±0.36	*UVOT*	
2025-01-29T05:15:58	60704.219	0.021	30.829	*uvw2*	>21.06	>20.81	*UVOT*	
2025-01-29T05:16:09	60704.220	0.022	31.012	*u*	17.76±0.16	17.61±0.16	*UVOT*	x
2025-01-29T05:16:23	60704.220	0.022	31.246	*v*	17.45±0.44	17.36±0.44	*UVOT*	x
2025-01-29T06:11:33	60704.258	0.060	86.405	*b*	17.56±0.32	17.43±0.32	*UVOT*	x
2025-01-29T06:14:13	60704.260	0.062	89.080	*b*	17.56±0.06	17.43±0.06	*UVOT*	x
2025-01-29T06:17:38	60704.262	0.064	92.492	*white*	18.42±0.06	18.27±0.06	*UVOT*	
2025-01-29T07:56:09	60704.331	0.133	191.002	*v*	17.97±0.08	17.87±0.08	*UVOT*	x
2025-01-29T09:24:31	60704.392	0.194	279.381	*b*	17.48±0.06	17.35±0.06	*UVOT*	x
2025-01-29T11:00:21	60704.459	0.261	375.207	*uvm2*	>24.78	>24.52	*UVOT*	
2025-01-29T11:11:42	60704.466	0.268	386.551	*uvw1*	20.14±0.13	19.93±0.13	*UVOT*	
2025-01-29T12:34:14	60704.524	0.326	469.097	*u*	18.42±0.06	18.27±0.06	*UVOT*	x
2025-01-29T12:49:19	60704.534	0.336	484.179	*b*	18.05±0.06	17.93±0.06	*UVOT*	x
2025-01-29T15:42:35	60704.655	0.457	657.449	*uvw1*	21.59±0.28	21.38±0.28	*UVOT*	
2025-01-29T15:57:33	60704.665	0.467	672.403	*u*	19.20±0.06	19.05±0.06	*UVOT*	x
2025-01-29T18:47:18	60704.783	0.585	842.152	*b*	19.03±0.18	18.91±0.18	*UVOT*	x
2025-01-30T02:50:30	60705.118	0.920	1325.356	*u*	20.08±0.17	19.92±0.17	*UVOT*	x
2025-01-30T02:55:56	60705.122	0.924	1330.799	*white*	20.57±0.13	20.42±0.13	*UVOT*	
2025-01-30T03:04:06	60705.128	0.930	1338.952	*v*	19.20±0.32	19.11±0.32	*UVOT*	x
2025-01-30T12:18:01	60705.513	1.314	1892.873	*white*	20.48±0.13	20.33±0.13	*UVOT*	
2025-01-31T10:02:37	60706.418	2.220	3197.471	*white*	21.17±0.12	21.01±0.12	*UVOT*	
2025-01-31T21:02:59	60706.877	2.679	3857.843	*white*	21.16±0.13	21.01±0.13	*UVOT*	

T_{start}		$T - T_{GRB}$		Filter	Magnitude	Corrected Magnitude	Telescope	Analysis
UT	MJD	Day	Minute					
(1)		(2)		(3)	(4)	(5)	(6)	(7)
2025-02-01T16:00:20	60707.667	3.469	4995.193	*white*	21.38±0.12	21.23±0.12	*UVOT*	
2025-02-01T19:48:07	60707.825	3.627	5222.977	*white*	21.81±0.16	21.66±0.16	*UVOT*	
2025-02-01T20:43:07	60707.863	3.665	5277.967	*white*	>23.00	>22.85	*UVOT*	
2025-02-06T13:16:46	60712.553	8.355	12031.617	*u*	22.61±0.36	22.46±0.36	*UVOT*	x
2025-02-09T13:15:24	60715.552	11.354	16350.256	*uvw1*	>23.00	22.79	*UVOT*	
2025-02-10T21:34:48	60716.899	12.701	18289.663	*u*	22.32±0.35	22.17±0.35	*UVOT*	x
B band								
2025-01-29T05:13:55	60704.218	0.020	28.770	*B*	17.27±0.07	17.14±0.07	Skynet	x
2025-01-29T05:16:31	60704.220	0.022	31.376	*B*	17.23±0.05	17.11±0.05	Skynet	x
2025-01-29T05:20:13	60704.222	0.024	35.077	*B*	17.30±0.06	17.18±0.06	Skynet	x
2025-01-29T05:26:09	60704.227	0.028	41.010	*B*	17.34±0.04	17.21±0.04	Skynet	x
2025-01-29T05:27:38	60704.228	0.030	42.493	*B*	17.29±0.04	17.16±0.04	Skynet	x
2025-01-29T05:35:46	60704.233	0.035	50.629	*B*	17.39±0.04	17.26±0.04	Skynet	x
2025-01-29T05:36:01	60704.233	0.035	50.874	*B*	17.27±0.04	17.14±0.04	Skynet	x
2025-01-29T05:45:38	60704.240	0.042	60.493	*B*	17.40±0.04	17.27±0.04	Skynet	x
2025-01-29T05:47:59	60704.242	0.044	62.840	*B*	17.47±0.03	17.34±0.03	Skynet	x
2025-01-29T05:56:54	60704.248	0.050	71.754	*B*	17.39±0.03	17.26±0.03	Skynet	x
2025-01-29T06:02:16	60704.252	0.054	77.125	*B*	17.44±0.03	17.32±0.03	Skynet	x
2025-01-29T06:10:05	60704.257	0.059	84.944	*B*	17.44±0.04	17.32±0.04	Skynet	x
2025-01-29T06:18:39	60704.263	0.065	93.512	*B*	17.59±0.03	17.47±0.03	Skynet	x
2025-01-29T06:29:53	60704.271	0.073	104.744	*B*	17.64±0.03	17.52±0.03	Skynet	x
2025-01-29T06:38:09	60704.277	0.078	113.010	*B*	17.66±0.03	17.54±0.03	Skynet	x
2025-01-29T07:51:06	60704.327	0.129	185.960	*B*	18.32±0.06	18.20±0.06	Skynet	x
2025-01-29T08:33:24	60704.357	0.159	228.253	*B*	17.87±0.04	17.75±0.04	Skynet	x
g' band								
2025-01-29T20:15:56	60704.844	0.646	930.783	g'	19.21±0.03	19.09±0.03	TNOT	x
2025-01-30T01:05:00	60705.045	0.847	1219.853	g'	19.40±0.06	19.28±0.06	KAO	x
2025-01-30T05:53:59	60705.246	1.048	1508.837	g'	18.94±0.04	18.82±0.04	KNC	x
2025-01-30T06:04:01	60705.253	1.055	1518.877	g'	19.00±0.05	18.89±0.05	KNC	x
2025-01-30T07:28:41	60705.312	1.114	1603.544	g'	19.16±0.05	19.04±0.05	KNC	x
2025-01-30T07:50:29	60705.327	1.129	1625.337	g'	19.11±0.05	18.99±0.05	KNC	x
2025-01-30T08:00:55	60705.334	1.136	1635.772	g'	19.23±0.05	19.11±0.05	KNC	x
2025-01-31T05:39:41	60706.236	2.038	2934.540	g'	20.63±0.14	20.52±0.14	KNC	x
2025-01-31T07:52:55	60706.328	2.130	3067.767	g'	20.28±0.12	20.16±0.12	KNC	x
2025-02-01T06:37:04	60707.276	3.078	4431.930	g'	20.52±0.12	20.41±0.12	KNC	x
2025-02-01T06:57:10	60707.290	3.092	4452.033	g'	20.65±0.13	20.53±0.13	KNC	x
2025-02-01T20:18:13	60707.846	3.648	5253.081	g'	20.79±0.15	20.68±0.15	KNC	x
2025-02-03T01:57:31	60709.082	4.884	7032.368	g'	21.35±0.10	21.23±0.10	NAO-2m	x
2025-02-04T00:48:59	60710.034	5.836	8403.838	g'	21.50±0.20	21.38±0.20	KNC	x
2025-02-04T02:42:14	60710.113	5.915	8517.089	g'	22.30±0.06	22.18±0.06	C2PU-O	x
2025-02-04T04:58:11	60710.207	6.009	8653.038	g'	22.47±0.08	22.35±0.08	Artemis	x
2025-02-05T04:57:09	60711.206	7.008	10092.016	g'	22.62±0.09	22.50±0.09	Artemis	x
2025-02-05T05:31:52	60711.230	7.032	10126.717	g'	22.60±0.25	22.48±0.25	PicduMidi/T1M	x
V band								
2025-01-29T05:14:45	60704.219	0.021	29.605	*V*	17.02±0.04	16.93±0.04	Skynet	x
2025-01-29T05:17:36	60704.221	0.023	32.456	*V*	16.96±0.03	16.86±0.03	Skynet	x
2025-01-29T05:21:19	60704.223	0.025	36.172	*V*	17.01±0.04	16.92±0.04	Skynet	x
2025-01-29T05:27:42	60704.228	0.030	42.551	*V*	17.03±0.03	16.93±0.03	Skynet	x
2025-01-29T05:28:57	60704.228	0.030	43.804	*V*	17.00±0.03	16.91±0.03	Skynet	x
2025-01-29T05:37:33	60704.234	0.036	52.415	*V*	17.07±0.03	16.98±0.03	Skynet	x
2025-01-29T05:37:39	60704.234	0.036	52.501	*V*	17.04±0.02	16.94±0.02	Skynet	x
2025-01-29T05:47:28	60704.241	0.043	62.322	*V*	17.13±0.02	17.04±0.02	Skynet	x
2025-01-29T05:50:17	60704.243	0.045	65.144	*V*	17.09±0.02	16.99±0.02	Skynet	x
2025-01-29T05:59:02	60704.249	0.051	73.885	*V*	17.24±0.02	17.15±0.02	Skynet	x
2025-01-29T06:05:07	60704.254	0.056	79.976	*V*	17.26±0.02	17.17±0.02	Skynet	x
2025-01-29T06:12:37	60704.259	0.061	87.479	*V*	17.25±0.02	17.16±0.02	Skynet	x
2025-01-29T06:22:06	60704.265	0.067	96.954	*V*	17.34±0.02	17.25±0.02	Skynet	x
2025-01-29T06:32:59	60704.273	0.075	107.840	*V*	17.45±0.02	17.36±0.02	Skynet	x
2025-01-29T06:42:17	60704.279	0.081	117.143	*V*	17.51±0.02	17.42±0.02	Skynet	x
2025-01-29T07:56:15	60704.331	0.133	191.116	*V*	18.01±0.04	17.92±0.04	Skynet	x
2025-01-29T08:39:52	60704.361	0.163	234.733	*V*	17.61±0.02	17.52±0.02	Skynet	x
2025-01-30T05:15:39	60705.219	1.021	1470.512	*V*	19.08±0.05	18.99±0.05	Skynet	x
2025-01-30T05:30:51	60705.230	1.032	1485.704	*V*	19.00±0.04	18.91±0.04	Skynet	x
2025-01-30T05:46:04	60705.240	1.042	1500.925	*V*	18.99±0.04	18.90±0.04	Skynet	x
2025-01-30T06:01:16	60705.251	1.053	1516.117	*V*	18.91±0.03	18.82±0.03	Skynet	x
2025-01-30T06:16:28	60705.261	1.063	1531.324	*V*	18.91±0.04	18.82±0.04	Skynet	x
2025-01-30T06:31:39	60705.272	1.074	1546.516	*V*	18.93±0.04	18.83±0.04	Skynet	x

T_{start}		$T - T_{GRB}$		Filter	Magnitude	Corrected Magnitude	Telescope	Analysis
UT	MJD	Day	Minute					
(1)		(2)		(3)	(4)	(5)	(6)	(7)
2025-01-30T06:46:52	60705.283	1.085	1561.722	V	19.04±0.04	18.95±0.04	Skynet	x
2025-01-30T07:02:04	60705.293	1.095	1576.928	V	19.17±0.04	19.08±0.04	Skynet	x
2025-01-30T07:17:16	60705.304	1.106	1592.120	V	19.28±0.05	19.19±0.05	Skynet	x
2025-01-30T07:32:27	60705.314	1.116	1607.312	V	19.23±0.05	19.14±0.05	Skynet	x
2025-01-30T07:45:08	60705.323	1.125	1619.999	V	19.27±0.05	19.17±0.05	Skynet	x
2025-01-30T08:02:49	60705.335	1.137	1637.682	V	19.26±0.05	19.16±0.05	Skynet	x
2025-01-30T08:18:02	60705.346	1.148	1652.888	V	19.23±0.05	19.13±0.05	Skynet	x
2025-01-30T08:35:46	60705.358	1.160	1670.629	V	19.20±0.04	19.10±0.04	Skynet	x
2025-02-01T05:56:31	60707.248	3.050	4391.380	V	20.94±0.07	20.85±0.07	Skynet	x
2025-02-01T07:47:57	60707.325	3.127	4502.807	V	21.17±0.07	21.08±0.07	Skynet	x
r' band								
2025-01-29T20:34:41	60704.857	0.659	949.550	r'	18.96±0.05	18.88±0.05	TNOT	x
2025-01-30T01:17:48	60705.054	0.856	1232.666	r'	19.17±0.05	19.09±0.05	KAO	x
2025-01-30T06:14:06	60705.260	1.062	1528.956	r'	18.71±0.06	18.63±0.06	KNC	x
2025-01-30T07:40:07	60705.320	1.122	1614.977	r'	18.90±0.05	18.82±0.05	KNC	x
2025-01-30T08:08:34	60705.339	1.141	1643.425	r'	18.96±0.03	18.88±0.03	COLIBRI-VIS	x
2025-01-30T09:22:49	60705.391	1.193	1717.681	r'	18.99±0.04	18.91±0.04	COLIBRI-VIS	x
2025-01-30T11:30:56	60705.480	1.282	1845.797	r'	19.22±0.03	19.14±0.03	COLIBRI-VIS	x
2025-01-31T05:49:56	60706.243	2.045	2944.787	r'	19.94±0.12	19.86±0.12	KNC	x
2025-01-31T08:08:01	60706.339	2.141	3082.871	r'	20.33±0.05	20.25±0.05	COLIBRI-VIS	x
2025-01-31T08:24:30	60706.350	2.152	3099.361	r'	20.47±0.08	20.39±0.08	COLIBRI-VIS	x
2025-01-31T10:16:49	60706.428	2.230	3211.681	r'	20.71±0.09	20.63±0.09	COLIBRI-VIS	x
2025-01-31T11:59:50	60706.500	2.302	3314.691	r'	20.51±0.05	20.43±0.05	COLIBRI-VIS	x
2025-02-01T07:21:03	60707.306	3.108	4475.900	r'	20.43±0.10	20.35±0.10	KNC	x
2025-02-01T08:34:39	60707.357	3.159	4549.501	r'	20.52±0.06	20.45±0.06	COLIBRI-VIS	x
2025-02-01T11:29:39	60707.479	3.281	4724.515	r'	20.56±0.05	20.48±0.05	COLIBRI-VIS	x
2025-02-02T08:05:45	60708.337	4.139	5960.601	r'	21.45±0.20	21.37±0.20	COLIBRI-VIS	x
2025-02-02T12:00:15	60708.500	4.302	6195.103	r'	21.53±0.12	21.45±0.12	COLIBRI-VIS	x
2025-02-03T03:34:41	60709.149	4.951	7129.546	r'	21.86±0.07	21.78±0.07	NAO-2m	x
2025-02-03T04:40:51	60709.195	4.997	7195.706	r'	21.76±0.14	21.68±0.14	OHP/MISTRAL	x
2025-02-03T08:11:50	60709.342	5.144	7406.689	r'	21.87±0.10	21.79±0.10	COLIBRI-VIS	x
2025-02-03T12:00:38	60709.500	5.302	7635.497	r'	21.99±0.10	21.91±0.10	COLIBRI-VIS	x
2025-02-04T05:20:12	60710.222	6.024	8675.057	r'	22.19±0.10	22.11±0.10	Artemis	x
2025-02-04T07:34:16	60710.315	6.117	8809.120	r'	22.36±0.17	22.28±0.17	COLIBRI-VIS	x
2025-02-05T04:36:52	60711.192	6.994	10071.733	r'	22.50±0.11	22.42±0.11	PicduMidi/T1M	x
2025-02-05T05:18:36	60711.221	7.023	10113.455	r'	22.27±0.09	22.19±0.09	Artemis	x
2025-02-05T10:31:09	60711.438	7.240	10426.002	r'	22.44±0.10	22.36±0.10	COLIBRI-VIS	x
2025-02-06T01:59:45	60712.083	7.885	11354.606	r'	22.34±0.14	22.26±0.14	PicduMidi/T1M	x
2025-02-06T10:59:27	60712.458	8.260	11894.302	r'	22.44±0.07	22.36±0.07	COLIBRI-VIS	x
2025-02-07T10:58:37	60713.457	9.259	13333.474	r'	22.70±0.12	22.62±0.12	COLIBRI-VIS	x
2025-02-08T10:01:36	60714.418	10.220	14716.456	r'	22.78±0.10	22.70±0.10	COLIBRI-VIS	x
2025-02-09T10:00:12	60715.417	11.219	16155.065	r'	22.68±0.10	22.60±0.10	COLIBRI-VIS	x
2025-02-10T10:03:01	60716.419	12.221	17597.879	r'	23.04±0.13	>22.96±0.13	COLIBRI-VIS	x
2025-02-19T11:18:58	60725.472	21.273	30633.824	r'	23.50±0.09	23.42±0.09	COLIBRI-VIS	x
2025-02-22T10:21:21	60728.431	24.233	34896.206	r'	23.71±0.10	23.63±0.10	COLIBRI-VIS	x
R band								
2025-01-29T04:47:00	60704.199	0.001	1.866	R	>17.49±	>17.42±	TAROT/TCH	x
2025-01-29T04:47:12	60704.199	0.001	2.067	R	>17.32±	>17.25±	TAROT/TCH	x
2025-01-29T04:47:25	60704.200	0.002	2.267	R	16.92±0.40	16.85±0.40	TAROT/TCH	x
2025-01-29T04:47:37	60704.200	0.002	2.467	R	17.12±0.40	17.05±0.40	TAROT/TCH	x
2025-01-29T04:47:49	60704.200	0.002	2.667	R	16.92±0.40	16.85±0.40	TAROT/TCH	x
2025-01-29T04:48:59	60704.201	0.003	3.844	R	17.35±0.16	17.27±0.16	TAROT/TCH	x
2025-01-29T04:49:40	60704.201	0.003	4.520	R	17.71±0.23	17.63±0.23	TAROT/TCH	x
2025-01-29T04:50:19	60704.202	0.004	5.168	R	18.24±0.37	18.16±0.37	TAROT/TCH	x
2025-01-29T04:50:58	60704.202	0.004	5.831	R	18.12±0.32	18.04±0.32	TAROT/TCH	x
2025-01-29T04:52:21	60704.203	0.005	7.213	R	17.58±0.12	17.50±0.12	TAROT/TCH	x
2025-01-29T04:54:01	60704.204	0.006	8.869	R	17.66±0.13	17.59±0.13	TAROT/TCH	x
2025-01-29T04:55:40	60704.205	0.007	10.525	R	17.45±0.10	17.38±0.10	TAROT/TCH	x
2025-01-29T04:56:53	60704.206	0.008	11.735	R	17.20±0.14	17.13±0.14	FRAM-Auger	x
2025-01-29T04:57:50	60704.207	0.009	12.700	R	17.16±0.08	17.09±0.08	TAROT/TCH	x
2025-01-29T04:59:30	60704.208	0.010	14.356	R	17.02±0.07	16.95±0.07	TAROT/TCH	x
2025-01-29T05:01:09	60704.209	0.011	16.012	R	17.06±0.07	16.99±0.07	TAROT/TCH	x
2025-01-29T05:02:49	60704.210	0.012	17.668	R	16.79±0.09	16.71±0.09	FRAM-Auger	x
2025-01-29T05:03:39	60704.211	0.013	18.503	R	17.02±0.05	16.94±0.05	TAROT/TCH	x
2025-01-29T05:06:48	60704.213	0.015	21.656	R	16.93±0.04	16.85±0.04	TAROT/TCH	x
2025-01-29T05:08:45	60704.214	0.016	23.600	R	16.78±0.07	16.70±0.07	FRAM-Auger	x
2025-01-29T05:09:56	60704.215	0.017	24.796	R	16.93±0.05	16.86±0.05	TAROT/TCH	x

T_{start}		$T - T_{GRB}$		Filter	Magnitude	Corrected Magnitude	Telescope	Analysis
UT	MJD	Day	Minute					
(1)		(2)		(3)	(4)	(5)	(6)	(7)
2025-01-29T05:13:41	60704.218	0.020	28.540	*R*	16.86±0.07	16.79±0.07	Skynet	x
2025-01-29T05:14:43	60704.219	0.021	29.576	*R*	16.77±0.05	16.70±0.05	Skynet	x
2025-01-29T05:17:01	60704.220	0.022	31.880	*R*	16.81±0.06	16.74±0.06	Skynet	x
2025-01-29T05:20:06	60704.222	0.024	34.962	*R*	16.82±0.06	16.75±0.06	Skynet	x
2025-01-29T05:20:30	60704.223	0.025	35.351	*R*	16.84±0.07	16.77±0.07	FRAM-Auger	x
2025-01-29T05:22:01	60704.224	0.026	36.877	*R*	16.84±0.05	16.77±0.05	Skynet	x
2025-01-29T05:24:00	60704.225	0.027	38.864	*R*	16.79±0.05	16.72±0.05	Skynet	x
2025-01-29T05:24:02	60704.225	0.027	38.893	*R*	16.84±0.04	16.77±0.04	TAROT/TCH	x
2025-01-29T05:26:29	60704.227	0.029	41.341	*R*	16.79±0.04	16.72±0.04	Skynet	x
2025-01-29T05:27:12	60704.227	0.029	42.061	*R*	16.89±0.04	16.82±0.04	TAROT/TCH	x
2025-01-29T05:27:40	60704.228	0.030	42.522	*R*	16.82±0.05	16.75±0.05	Skynet	x
2025-01-29T05:30:21	60704.229	0.031	45.215	*R*	16.87±0.04	16.80±0.04	TAROT/TCH	x
2025-01-29T05:30:57	60704.230	0.032	45.805	*R*	16.80±0.04	16.73±0.04	Skynet	x
2025-01-29T05:31:59	60704.231	0.033	46.842	*R*	16.89±0.04	16.82±0.04	Skynet	x
2025-01-29T05:32:28	60704.231	0.033	47.317	*R*	16.88±0.07	16.81±0.07	FRAM-Auger	x
2025-01-29T05:33:46	60704.232	0.034	48.628	*R*	16.80±0.03	16.73±0.03	TAROT/TCH	x
2025-01-29T05:36:02	60704.233	0.035	50.888	*R*	16.78±0.04	16.71±0.04	Skynet	x
2025-01-29T05:36:16	60704.234	0.036	51.133	*R*	16.87±0.04	16.79±0.04	Skynet	x
2025-01-29T05:36:55	60704.234	0.036	51.781	*R*	16.84±0.03	16.77±0.03	TAROT/TCH	x
2025-01-29T05:40:05	60704.236	0.038	54.935	*R*	16.91±0.03	16.83±0.03	TAROT/TCH	x
2025-01-29T05:40:56	60704.237	0.039	55.799	*R*	16.93±0.04	16.86±0.04	Skynet	x
2025-01-29T05:41:47	60704.237	0.039	56.648	*R*	16.86±0.03	16.79±0.03	Skynet	x
2025-01-29T05:43:31	60704.239	0.041	58.376	*R*	16.94±0.03	16.87±0.03	TAROT/TCH	x
2025-01-29T05:43:31	60704.239	0.041	58.376	*R*	16.92±0.03	16.84±0.03	TAROT/TCH	x
2025-01-29T05:45:57	60704.240	0.042	60.810	*R*	16.89±0.04	16.82±0.04	Skynet	x
2025-01-29T05:47:46	60704.242	0.043	62.624	*R*	16.92±0.03	16.85±0.03	Skynet	x
2025-01-29T05:49:50	60704.243	0.045	64.684	*R*	16.92±0.04	16.85±0.04	TAROT/TCH	x
2025-01-29T05:50:18	60704.243	0.045	65.159	*R*	17.07±0.08	17.00±0.08	FRAM-Auger	x
2025-01-29T05:51:25	60704.244	0.046	66.282	*R*	16.95±0.04	16.88±0.04	Skynet	x
2025-01-29T05:53:20	60704.245	0.047	68.197	*R*	16.93±0.03	16.86±0.03	TAROT/TCH	x
2025-01-29T05:55:52	60704.247	0.049	70.732	*R*	16.98±0.03	16.91±0.03	Skynet	x
2025-01-29T05:56:30	60704.248	0.050	71.365	*R*	16.99±0.03	16.91±0.03	TAROT/TCH	x
2025-01-29T05:57:16	60704.248	0.050	72.128	*R*	16.99±0.04	16.92±0.04	Skynet	x
2025-01-29T05:59:40	60704.250	0.052	74.519	*R*	17.04±0.04	16.97±0.04	TAROT/TCH	x
2025-01-29T06:02:57	60704.252	0.054	77.816	*R*	17.05±0.03	16.98±0.03	TAROT/TCH	x
2025-01-29T06:03:01	60704.252	0.054	77.874	*R*	17.03±0.03	16.96±0.03	Skynet	x
2025-01-29T06:03:40	60704.253	0.055	78.522	*R*	17.07±0.04	17.00±0.04	Skynet	x
2025-01-29T06:06:08	60704.254	0.056	80.984	*R*	17.00±0.04	16.92±0.04	TAROT/TCH	x
2025-01-29T06:07:50	60704.255	0.057	82.684	*R*	17.19±0.08	17.12±0.08	FRAM-Auger	x
2025-01-29T06:09:17	60704.256	0.058	84.138	*R*	17.10±0.04	17.03±0.04	TAROT/TCH	x
2025-01-29T06:10:35	60704.257	0.059	85.434	*R*	17.12±0.04	17.05±0.04	Skynet	x
2025-01-29T06:10:58	60704.258	0.060	85.823	*R*	17.19±0.03	17.12±0.03	Skynet	x
2025-01-29T06:15:51	60704.261	0.063	90.704	*R*	17.15±0.04	17.07±0.04	TAROT/TCH	x
2025-01-29T06:15:51	60704.261	0.063	90.704	*R*	17.07±0.03	17.00±0.03	TAROT/TCH	x
2025-01-29T06:18:00	60704.263	0.064	92.864	*R*	17.24±0.03	17.17±0.03	Skynet	x
2025-01-29T06:19:00	60704.263	0.065	93.858	*R*	17.17±0.04	17.10±0.04	TAROT/TCH	x
2025-01-29T06:19:37	60704.264	0.066	94.477	*R*	17.16±0.03	17.09±0.03	Skynet	x
2025-01-29T06:22:34	60704.266	0.068	97.429	*R*	17.18±0.04	17.11±0.04	TAROT/TCH	x
2025-01-29T06:25:44	60704.268	0.070	100.597	*R*	17.19±0.03	17.11±0.03	TAROT/TCH	x
2025-01-29T06:26:04	60704.268	0.070	100.928	*R*	17.25±0.04	17.18±0.04	Skynet	x
2025-01-29T06:28:54	60704.270	0.072	103.751	*R*	17.18±0.04	17.11±0.04	TAROT/TCH	x
2025-01-29T06:29:08	60704.270	0.072	103.996	*R*	17.26±0.03	17.19±0.03	Skynet	x
2025-01-29T06:31:18	60704.272	0.074	106.156	*R*	17.25±0.08	17.18±0.08	FRAM-Auger	x
2025-01-29T06:34:48	60704.274	0.076	109.655	*R*	17.28±0.03	17.21±0.03	Skynet	x
2025-01-29T06:39:41	60704.278	0.080	114.536	*R*	17.33±0.03	17.26±0.03	Skynet	x
2025-01-29T06:39:57	60704.278	0.080	114.810	*R*	17.30±0.04	17.23±0.04	TAROT/TCH	x
2025-01-29T06:43:07	60704.280	0.082	117.978	*R*	17.37±0.04	17.30±0.04	TAROT/TCH	x
2025-01-29T06:44:15	60704.281	0.083	119.101	*R*	17.35±0.03	17.28±0.03	Skynet	x
2025-01-29T06:46:16	60704.282	0.084	121.132	*R*	17.33±0.04	17.25±0.04	TAROT/TCH	x
2025-01-29T06:54:59	60704.288	0.090	129.844	*R*	17.51±0.10	17.43±0.10	FRAM-Auger	x
2025-01-29T07:17:48	60704.304	0.106	152.653	*R*	17.51±0.04	17.44±0.04	Skynet	x
2025-01-29T07:21:14	60704.306	0.108	156.095	*R*	17.59±0.05	17.51±0.05	TAROT/TCH	x
2025-01-29T07:24:23	60704.309	0.111	159.248	*R*	17.59±0.04	17.52±0.04	TAROT/TCH	x
2025-01-29T07:27:33	60704.311	0.113	162.402	*R*	17.63±0.04	17.55±0.04	TAROT/TCH	x
2025-01-29T07:40:50	60704.320	0.122	175.693	*R*	17.79±0.05	17.72±0.05	TAROT/TCH	x
2025-01-29T07:44:00	60704.322	0.124	178.861	*R*	17.68±0.04	17.61±0.04	TAROT/TCH	x
2025-01-29T07:47:09	60704.324	0.126	182.015	*R*	17.72±0.05	17.65±0.05	TAROT/TCH	x

T_{start}		$T - T_{GRB}$		Filter	Magnitude	Corrected Magnitude	Telescope	Analysis
UT	MJD	Day	Minute					
(1)		(2)		(3)	(4)	(5)	(6)	(7)
2025-01-29T08:00:14	60704.334	0.135	195.090	*R*	17.87±0.05	17.80±0.05	TAROT/TCH	x
2025-01-29T08:00:16	60704.334	0.135	195.119	*R*	17.94±0.04	17.87±0.04	Skynet	x
2025-01-29T08:03:23	60704.336	0.138	198.244	*R*	17.85±0.05	17.77±0.05	TAROT/TCH	x
2025-01-29T08:06:32	60704.338	0.140	201.397	*R*	17.86±0.05	17.79±0.05	TAROT/TCH	x
2025-01-29T08:44:55	60704.365	0.167	239.773	*R*	17.43±0.02	17.36±0.02	Skynet	x
2025-01-29T09:27:18	60704.394	0.196	282.152	*R*	17.13±0.05	17.05±0.05	KAIT	x
2025-01-29T09:32:03	60704.397	0.199	286.904	*R*	16.78±0.05	16.71±0.05	KAIT	x
2025-01-29T09:36:46	60704.401	0.203	291.628	*R*	16.63±0.05	16.56±0.05	KAIT	x
2025-01-29T09:36:49	60704.401	0.203	291.671	*R*	16.65±0.05	16.58±0.05	Skynet	x
2025-01-29T09:41:31	60704.404	0.206	296.380	*R*	16.48±0.05	16.41±0.05	KAIT	x
2025-01-29T09:46:17	60704.407	0.209	301.146	*R*	16.47±0.05	16.40±0.05	KAIT	x
2025-01-29T09:52:18	60704.411	0.213	307.151	*R*	16.62±0.05	16.55±0.05	Skynet	x
2025-01-29T09:55:49	60704.414	0.216	310.679	*R*	16.45±0.05	16.38±0.05	KAIT	x
2025-01-29T10:00:33	60704.417	0.219	315.402	*R*	16.47±0.05	16.40±0.05	KAIT	x
2025-01-29T10:05:45	60704.421	0.223	320.600	*R*	16.58±0.05	16.51±0.05	KAIT	x
2025-01-29T10:10:28	60704.424	0.226	325.324	*R*	16.71±0.05	16.64±0.05	KAIT	x
2025-01-29T10:12:56	60704.426	0.228	327.786	*R*	16.87±0.06	16.80±0.06	Skynet	x
2025-01-29T10:15:12	60704.427	0.229	330.061	*R*	16.82±0.05	16.75±0.05	KAIT	x
2025-01-29T10:18:06	60704.429	0.231	332.956	*R*	16.92±0.06	16.85±0.06	Skynet	x
2025-01-29T10:20:00	60704.431	0.233	334.856	*R*	16.94±0.05	16.87±0.05	KAIT	x
2025-01-29T10:24:45	60704.434	0.236	339.608	*R*	16.99±0.05	16.92±0.05	KAIT	x
2025-01-29T10:29:32	60704.437	0.239	344.389	*R*	17.03±0.05	16.96±0.05	KAIT	x
2025-01-29T10:34:17	60704.440	0.242	349.141	*R*	17.03±0.05	16.96±0.05	KAIT	x
2025-01-29T10:41:38	60704.446	0.248	356.500	*R*	17.05±0.05	16.98±0.05	KAIT	x
2025-01-29T10:51:22	60704.452	0.254	366.220	*R*	17.09±0.05	17.02±0.05	KAIT	x
2025-01-29T11:00:52	60704.459	0.261	375.724	*R*	17.16±0.05	17.09±0.05	KAIT	x
2025-01-29T11:10:25	60704.466	0.268	385.271	*R*	17.16±0.05	17.09±0.05	KAIT	x
2025-01-29T11:20:06	60704.472	0.274	394.962	*R*	17.20±0.05	17.13±0.05	KAIT	x
2025-01-29T11:29:49	60704.479	0.281	404.682	*R*	17.26±0.05	17.19±0.05	KAIT	x
2025-01-29T11:40:31	60704.486	0.288	415.367	*R*	17.32±0.05	17.25±0.05	KAIT	x
2025-01-29T11:52:31	60704.495	0.297	427.376	*R*	17.38±0.05	17.31±0.05	KAIT	x
2025-01-30T00:20:54	60705.015	0.816	1175.759	*R*	19.17±0.06	19.10±0.06	Skynet	x
2025-01-30T01:03:57	60705.044	0.846	1218.800	*R*	19.26±0.06	19.19±0.06	Skynet	x
2025-01-30T02:36:01	60705.108	0.910	1310.874	*R*	19.28±0.06	19.21±0.06	Skynet	x
2025-01-30T03:14:31	60705.135	0.937	1349.380	*R*	19.32±0.09	19.25±0.09	Skynet	x
2025-01-30T03:50:28	60705.160	0.962	1385.322	*R*	19.30±0.06	19.23±0.06	Skynet	x
2025-01-30T04:16:09	60705.178	0.980	1411.012	*R*	19.46±0.07	19.39±0.07	Skynet	x
2025-01-30T05:30:50	60705.230	1.032	1485.690	*R*	18.71±0.03	18.64±0.03	Skynet	x
2025-01-30T05:45:56	60705.240	1.042	1500.796	*R*	18.71±0.03	18.64±0.03	Skynet	x
2025-01-30T06:31:13	60705.272	1.074	1546.069	*R*	18.82±0.02	18.75±0.02	Skynet	x
2025-01-30T07:01:24	60705.293	1.095	1576.252	*R*	18.93±0.03	18.86±0.03	Skynet	x
2025-01-30T07:46:41	60705.324	1.126	1621.540	*R*	18.99±0.03	18.92±0.03	Skynet	x
2025-01-30T08:34:28	60705.357	1.159	1669.319	*R*	18.88±0.02	18.81±0.02	Skynet	x
2025-01-30T09:22:02	60705.390	1.192	1716.896	*R*	18.86±0.05	18.79±0.05	KAIT	x
2025-01-30T09:39:54	60705.403	1.205	1734.752	*R*	18.97±0.05	18.90±0.05	KAIT	x
2025-01-30T09:58:05	60705.415	1.217	1752.940	*R*	18.99±0.05	18.92±0.05	KAIT	x
2025-01-30T10:15:55	60705.428	1.230	1770.767	*R*	19.03±0.05	18.96±0.05	KAIT	x
2025-01-30T10:34:07	60705.440	1.242	1788.983	*R*	19.03±0.05	18.96±0.05	KAIT	x
2025-01-30T10:52:04	60705.453	1.255	1806.925	*R*	19.06±0.05	18.99±0.05	KAIT	x
2025-01-30T11:10:12	60705.465	1.267	1825.055	*R*	19.09±0.05	19.02±0.05	KAIT	x
2025-01-30T11:28:13	60705.478	1.280	1843.069	*R*	19.11±0.05	19.04±0.05	KAIT	x
2025-01-30T11:46:14	60705.490	1.292	1861.098	*R*	19.16±0.05	19.09±0.05	KAIT	x
2025-01-30T12:04:19	60705.503	1.305	1879.170	*R*	19.21±0.05	19.14±0.05	KAIT	x
2025-01-30T12:22:19	60705.516	1.317	1897.170	*R*	19.28±0.05	19.21±0.05	KAIT	x
2025-01-30T12:40:28	60705.528	1.330	1915.328	*R*	19.24±0.05	19.17±0.05	KAIT	x
2025-01-30T12:58:25	60705.541	1.343	1933.271	*R*	19.38±0.05	19.31±0.05	KAIT	x
2025-01-30T13:16:35	60705.553	1.355	1951.444	*R*	19.42±0.05	19.35±0.05	KAIT	x
2025-01-30T13:16:34	60705.553	1.355	1951.417	*R*	19.43±0.15	19.36±0.15	KNC	
2025-01-30T13:34:28	60705.566	1.368	1969.328	*R*	19.47±0.05	19.40±0.05	KAIT	x
2025-01-30T13:52:44	60705.578	1.380	1987.588	*R*	19.48±0.05	19.41±0.05	KAIT	x
2025-01-30T14:11:14	60705.591	1.393	2006.092	*R*	19.64±0.05	19.57±0.05	KAIT	x
2025-01-30T17:27:26	60705.727	1.529	2202.300	*R*	19.98±0.15	19.90±0.15	KNC	x
2025-01-30T22:16:50	60705.928	1.730	2491.683	*R*	20.00±0.10	19.93±0.10	AbAO-T70	x
2025-01-31T05:19:45	60706.222	2.024	2914.602	*R*	20.32±0.06	20.25±0.06	Skynet	x
2025-01-31T06:20:07	60706.264	2.066	2974.967	*R*	20.44±0.07	20.37±0.07	Skynet	x
2025-01-31T07:20:28	60706.306	2.108	3035.332	*R*	20.37±0.07	20.30±0.07	Skynet	x
2025-01-31T08:25:52	60706.351	2.153	3100.722	*R*	20.32±0.06	20.25±0.06	Skynet	x

T_{start}		$T - T_{GRB}$		Filter	Magnitude	Corrected Magnitude	Telescope	Analysis
UT	MJD	Day	Minute					
(1)		(2)		(3)	(4)	(5)	(6)	(7)
2025-01-31T23:10:05	60706.965	2.767	3984.933	R	20.44±0.11	20.37±0.11	AbAO-T70	x
2025-02-01T05:57:27	60707.248	3.050	4392.301	R	20.25±0.04	20.18±0.04	Skynet	x
2025-02-01T07:30:44	60707.313	3.115	4485.587	R	20.55±0.05	20.48±0.05	Euler	x
2025-02-01T07:48:04	60707.325	3.127	4502.922	R	20.49±0.04	20.42±0.04	Skynet	x
2025-02-02T07:20:42	60708.306	4.108	5915.562	R	21.06±0.10	20.99±0.10	Euler	x
2025-02-03T08:26:27	60709.352	5.154	7421.317	R	21.72±0.10	21.65±0.10	Euler	x
2025-02-05T08:58:33	60711.374	7.176	10333.416	R	22.79±0.11	22.72±0.11	Euler	x
2025-02-08T08:09:32	60714.340	10.142	14604.396	R	22.81±0.28	22.74±0.28	Euler	x
i' band								
2025-01-29T05:40:14	60704.236	0.038	55.083	i'	16.55±0.03	16.49±0.03	OHP/MISTRAL	x
2025-01-30T01:30:37	60705.063	0.865	1245.483	i'	18.92±0.03	18.86±0.03	KAO	x
2025-01-30T06:34:13	60705.274	1.076	1549.074	i'	18.53±0.11	18.48±0.11	KNC	x
2025-01-30T08:13:54	60705.343	1.145	1648.755	i'	18.75±0.12	18.69±0.12	KNC	x
2025-02-01T07:44:08	60707.322	3.124	4498.999	i'	20.17±0.05	20.11±0.05	Euler	x
2025-02-02T07:34:06	60708.315	4.117	5928.956	i'	21.00±0.06	20.94±0.06	Euler	x
2025-02-03T02:04:30	60709.086	4.888	7039.353	i'	21.30±0.10	21.24±0.10	NAO-2m	x
2025-02-03T08:39:54	60709.361	5.163	7434.761	i'	21.75±0.10	21.69±0.10	Euler	x
2025-02-04T03:18:10	60710.138	5.940	8553.025	i'	21.80±0.11	21.74±0.11	C2PU-O	x
2025-02-05T09:10:24	60711.382	7.184	10345.261	i'	22.45±0.20	22.39±0.20	Euler	x
2025-02-08T08:33:00	60714.356	10.158	14627.866	i'	>22.25±	>22.19±	Euler	x
I band								
2025-01-29T05:15:46	60704.219	0.021	30.628	I	16.69±0.07	16.64±0.07	Skynet	x
2025-01-29T05:22:34	60704.224	0.026	37.424	I	16.56±0.05	16.51±0.05	Skynet	x
2025-01-29T05:30:34	60704.230	0.032	45.431	I	16.63±0.05	16.58±0.05	Skynet	x
2025-01-29T05:39:17	60704.236	0.038	54.143	I	16.74±0.05	16.69±0.05	Skynet	x
2025-01-29T05:49:29	60704.243	0.045	64.338	I	16.70±0.04	16.65±0.04	Skynet	x
2025-01-29T06:01:24	60704.251	0.053	76.261	I	16.85±0.04	16.80±0.04	Skynet	x
2025-01-29T06:15:21	60704.261	0.063	90.215	I	16.98±0.04	16.93±0.04	Skynet	x
2025-01-29T06:36:20	60704.275	0.077	111.196	I	17.19±0.03	17.14±0.03	Skynet	x
2025-01-29T21:35:47	60704.900	0.702	1010.650	I	19.14±0.10	19.08±0.10	KNC	x
2025-01-30T01:19:13	60705.055	0.857	1234.067	I	18.97±0.11	18.91±0.11	KNC	x
2025-02-02T19:02:22	60708.793	4.595	6617.230	I	>20.69±	>20.64±	Generic	x
z band								
2025-02-04T02:59:50	60710.125	5.927	8534.685	z'	20.97±0.20	20.93±0.20	C2PU-O	x
2025-02-04T05:42:14	60710.238	6.040	8697.085	z'	21.81±0.16	21.77±0.16	Artemis	x
2025-02-05T05:41:13	60711.237	7.039	10136.076	z'	22.20±0.20	22.16±0.20	Artemis	x

Appendix E: Computation of the energy injection in NMMA

Energy Injection We introduce an energy injection parameter $\Delta \log_{10} E_0$ that starting from time $t_{\rm inj}$ linearly increases the log jet energy within the interval in NMMA and AFTERGLOWPY. $\Delta t_{\rm inj}$ from $\log_{10} E_0$ to $\log_{10} E_0 + \Delta \log_{10} E_0$ at time $t_{\rm inj} + \Delta t_{\rm inj}$, i.e.,

$$\log_{10} E_{\rm k,iso}(t) = \begin{cases} \log_{10} E_{\rm k,iso} & t < t_{\rm inj} \\ \log_{10} E_{\rm k,iso} + \Delta \log_{10} E \frac{t - t_{\rm inj}}{\Delta t_{\rm inj}} & t_{\rm inj} < t < t_{\rm inj} + \Delta t_{\rm inj} \\ \log_{10} E_{\rm k,iso} + \Delta \log_{10} E & t > t_{\rm inj} + \Delta t_{\rm inj}, \end{cases} \tag{E.1}$$

Likelihood function definition To infer the posterior $p(\vec{\theta}|d)$ from the light curve data d, we sample the parameter space of the model using the nested sampling algorithm as implemented in PYMULTINEST (Feroz et al. 2009; Buchner et al. 2014). In particular, we use the likelihood function $\ln \mathcal{L}(\vec{\theta}|d)$ (see Appendix E for further details on its computation)

$$\ln \mathcal{L}(\vec{\theta}|d) = \sum_{t_j} \left(-\frac{1}{2} \frac{(m(t_j) - m^\star(t_j, \vec{\theta}))^2}{\sigma(t_j)^2 + \sigma_{\rm sys}^2} + \ln(2\pi(\sigma(t_j)^2 + \sigma_{\rm sys}^2)) \right). \tag{E.2}$$

This likelihood function compares the observed magnitudes $m(t_j)$ at times t_j to the model predictions $m^\star(t_j, \vec{\theta})$ from AFTERGLOWPY. Here, $\sigma(t_j)$ represents the measurement uncertainties, and $\sigma_{\rm sys}$ denotes the systematic uncertainty.

Average chi-squared statistic Using posterior light curves derived from the "early time" data, we compute the average chi-squared statistic, $\langle \chi_j^2 \rangle$, for each data point d_j:

$$\langle \chi_j^2 \rangle = \int \left[\frac{(m(t_j) - m^\star(t_j, \vec{\theta}))^2}{\sigma(t_j)^2 + \sigma_{\rm sys}^2} \right] p(\vec{\theta}|d) d\vec{\theta}, \tag{E.3}$$